Quasiparticle Dynamics in Epitaxial Al-InAs Planar Josephson Junctions

Bassel Heiba Elfeky,[1,†] William M. Strickland,[1,†] Jaewoo Lee,[1] James T. Farmer,[2] Sadman Shanto,[2] Azarin Zarassi,[2] Dylan Langone,[1] Maxim G. Vavilov,[3] Eli M. Levenson-Falk,[2] and Javad Shabani[1,*]

[1] *Center for Quantum Information Physics, Department of Physics, New York University, New York 10003, USA*
[2] *Department of Physics, University of Southern California and Center for Quantum Information Science and Technology, University of Southern California, Los Angeles, California 90089, USA*
[3] *Department of Physics and Wisconsin Quantum Institute, University of Wisconsin-Madison, Madison, Wisconsin 53706, USA*

(Received 16 March 2023; accepted 18 August 2023; published 22 September 2023)

Quasiparticle (QP) effects play a significant role in the coherence and fidelity of superconducting quantum circuits. The Andreev bound states of high-transparency Josephson junctions can act as low-energy traps for QPs, providing a mechanism for studying the dynamics and properties of both the QPs and the junction. Using locally injected and thermal QPs, we study QP loss and QP poisoning in epitaxial Al-InAs Josephson junctions incorporated in a superconducting quantum interference device (SQUID) galvanically shorting a superconducting resonator to ground. We observe changes in the resonance line shape and frequency shifts consistent with QP trapping into and clearing out of the ABSs of the junctions when the junctions are phase biased. By monitoring the QP trapping and clearing mechanisms in time, we find a time scale of $\mathcal{O}(1\ \mu s)$ for these QP dynamics, consistent with the presence of phonon-mediated QP-QP interactions. Our measurements suggest that electron-phonon interactions play a significant role in the relaxation mechanisms of our system, while electron-photon interactions and electron-phonon interactions govern the clearing mechanisms. Our results highlight the QP-induced dissipation and complex QP dynamics in superconducting quantum circuits fabricated on superconductor-semiconductor heterostructures.

DOI: 10.1103/PRXQuantum.4.030339

I. INTRODUCTION

The presence of quasiparticles (QPs) in superconducting materials can prove detrimental to the operation of superconducting quantum circuits, where QP transport and tunneling can cause dissipation [1–6] and be a major source of decoherence in charge and parity-based qubits [7,8]. Even at low temperatures, significant densities of nonequilibrium QPs have been observed in superconducting films [1,4,5,9–11] due to Cooper-pair breaking caused by, e.g., leakage of infrared photons [12], cosmic rays [2,13–15], and material defects [16]. At low QP densities, studies have shown that the dominant mechanism for QP relaxation is the diffusive propagation of QPs through the superconductor [17], where they can eventually get trapped in defects or vortices [18–20]. At high QP densities, QP recombination involving phonon emission becomes the dominant mechanism for QP relaxation, where the emitted phonons can travel through the substrate before getting absorbed by the superconductor and breaking up Cooper pairs into new QPs [20–22].

Recently, novel superconductor-semiconductor structures have emerged as a promising platform to realize voltage-tunable wafer-scale superconducting circuit elements such as gatemon qubits [23–34], amplifiers [35], and couplers [36–39]. These material systems have also been studied for their potential application in topological fault-tolerant quantum computing [40–43]. In addition to the dissipation and qubit dephasing associated with QPs, in such fault-tolerant schemes, one must conduct braiding operations faster than the QP poisoning time to preserve the parity of the system [7,8]. Thus, understanding the dynamics and effects of QPs in hybrid superconductor-semiconductor structures is vital for the operation of qubits and other superconducting circuit elements on these structures.

*jshabani@nyu.edu
†These authors contributed equally to this work.

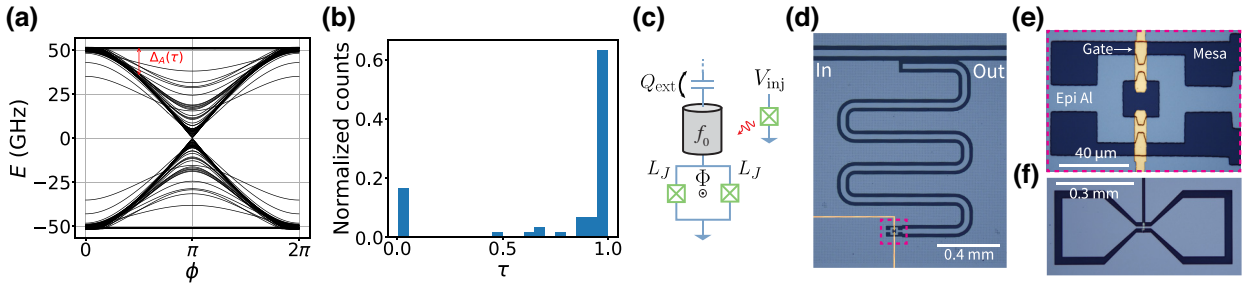

FIG. 1. The Andreev spectrum and the device design. (a) The calculated energy spectrum of the Andreev bound states in a wide Al-InAs junction. The results obtained are for a JJ with width $w = 1$ μm, normal region length $l = 100$ nm, length of the superconductor $l_{sc} = 2$ μm, superconducting gap $\Delta = 210$ μeV, carrier density $n = 4 \times 10^{11}$ cm^{-2}, and effective electron mass $m^* = 0.04m_e$, where m_e is the electron mass. (b) A histogram of the transparencies of the ABS modes in (a) extracted from fitting the modes to Eq. (1). (c) The circuit diagram of the CPW-SQUID device. A transmission-line resonator with frequency f_0 is coupled capacitively to a feed line characterized by an external quality factor Q_{ext} and directly connected to a superconducting loop with two Josephson junctions (JJs), each with inductance L_J. A flux Φ threads the loop. Separately, a two-terminal "injector" JJ is placed 1.6 mm away from the SQUID, serving to inject QPs to the circuit by biasing one terminal with voltage V_{inj} and grounding the other terminal. (d)–(f) Optical images of (d) the CPW-SQUID device, (e) the SQUID, and (f) the injector junction, where the etched mesa is shown in dark blue, epitaxial Al in light blue, and gates in gold.

In semiconductor-based Josephson junctions (JJs), supercurrent is carried by electrons and holes in conduction channels mediated by Andreev reflection [44]. Coherent Andreev reflections result in subgap Andreev bound states (ABSs), with each channel forming a pair of ABSs, having energy given by

$$E_A^{\pm}(\phi) = \pm\Delta\sqrt{1 - \tau\sin^2(\phi/2)}, \tag{1}$$

where ϕ, τ, and Δ are the phase difference across the junction, the transparency, and the superconducting gap, respectively. The energy spectrum of the ABSs in an Al-InAs JJ with width $w = 1$ μm, obtained using tight-binding simulations with realistic parameters (see Appendix A), is shown in Fig. 1(a). The simulations present an Andreev spectrum with a large number of modes and a few long junction modes, diffusive modes detached from the continuum at $\phi = 0$, present due to the wide nature of the planar JJ [45,46]. Fitting the modes in the Andreev spectrum to Eq. (1), we extract the transparencies (τ) of these modes and plot them as a histogram in Fig. 1(b), where we observe the majority of modes having high transparency and a small fraction of modes having intermediate transparency. Typically, at low temperatures, ABSs with energy E_A^- are occupied and those with energy E_A^+ are unoccupied. QPs, which have energy $\gtrsim \Delta$, can relax from the quasicontinuum into one of the Andreev levels, which effectively has a trap of depth $\Delta_A(\phi, \tau) = \Delta - E_A^+(\phi, \tau)$, as denoted in Fig. 1(a). Since ABSs with E_A^+ carry current in the opposite direction to those ABSs with E_A^-, a QP falling into the positive-energy ABS poisons the conduction channel resulting in the channel carrying zero supercurrent, a process known as QP poisoning. The resulting decrease in supercurrent and the corresponding increase in inductance can be read out using standard dispersive measurement techniques as demonstrated in Al-nanobridge JJs [47–49] and also in Al-InAs Josephson nanowires, where the spin state of a QP trapped in the Andreev level is used as the basis state of an Andreev spin qubit [31,32]. Trapped QPs can then be excited or cleared out of their Andreev traps by applying a high-frequency f_{clear} clearing tone with $hf_{clear} > \Delta_A$, where h is Planck's constant.

In this work, we study the trapping and clearing of QPs in epitaxial Al-InAs planar JJs embedded in a superconducting quantum interference device (SQUID) that electrically shorts a coplanar waveguide (CPW) resonator to ground. We show that by increasing the QP density through local QP injection or by raising the temperature, QPs can get trapped in the ABSs of the junctions at nonzero phase bias and we examine their effect on the resonance line shape. Further, we study the QP trapping and clearing dynamics by pulsing a clearing tone and measuring the time scales associated with the relaxation and excitation of QPs into and from the traps.

II. DEVICE DESIGN AND MEASUREMENT SETUP

The devices used in this study are fabricated on a superconductor-semiconductor (Al-InAs) heterostructure grown via molecular-beam epitaxy [50–53]. The weak link of the JJ is an InAs 2DEG grown near the surface and contacted *in situ* by a thin Al film. The heterostructure is grown on a 500-μm-thick InP substrate. We use an III-V wet etch to define the microwave circuit and an Al wet etch to define the JJ. A blanket layer of AlO_x is then deposited as a gate dielectric followed by a patterned layer of Al for the gate

electrodes, which are all kept grounded during the measurements. Further details on the growth and fabrication are provided in Appendix B.

Our device consists of a hanger $\lambda/4$ CPW resonator (with geometric inductance $L_0 = 1.573$ nH and capacitance $C_0 = 414$ fF) coupled capacitively to a common feed line, characterized by an external quality factor $Q_{\text{ext}} \approx 1440$. The resonator is shorted to ground through a SQUID with two symmetric JJs that are $w \approx 4$ μm wide and $l \approx 100$ nm long. We refer to the combined resonator-SQUID system as a CPW-SQUID. Coupled to the same feed line is a bare test resonator used for characterizing the Al film and two other CPW-SQUID devices, which we do not discuss in this work. Around the microwave circuit, we etch 2×2 μm holes in the ground plane on a 10-μm grid to act as flux-pinning holes. Near the microwave circuit, 1.6 mm away from the SQUID, we have a two-terminal JJ, fabricated on the same chip with the same junction structure, used for injecting QPs. By dc-voltage-biasing the "injector" JJ above twice the superconducting gap, $eV_{\text{bias}} > 2\Delta$, QPs are generated near the injector JJ area. These QPs can then relax to the gap edge or recombine, emitting phonons that propagate through the substrate breaking Cooper pairs successively, increasing the density of QPs in the circuit. A similar QP injection mechanism has been used in Refs. [20,54,55]. A circuit diagram of the CPW-SQUID device and injector junction is shown in Fig. 1(c) with optical micrographs shown in Figs. 1(d)–1(f).

The chip is measured in a dilution refrigerator at a temperature $T = 15$ mK, mounted on the mixing chamber in a QDevil QCage, a microwave-cavity sample holder with EMC-tight superconducting shielding. An out-of-plane magnetic field is applied to the chip using a superconducting coil placed inside the QCage shielding. All dc lines go through a QDevil QFilter, a low-pass filter with a resistance of 1.7 kΩ, such that the reported applied voltage bias to the injector V_{inj} is applied across the filter and the injector junction in series. We expand on the measurement setup in Appendix C. Unless specified otherwise, the measurements are all performed at a photon number of approximately 50. We first measure the complex transmission S_{21} and fit the resonant response in transmission to extract the resonant frequency f_r and the internal quality factor Q_{int}, using a fitting procedure outlined in Ref. [56]. Time-domain measurements are performed by applying a probe tone $f = f_r(\Phi/\Phi_0)$ and demodulating, 22-MHz low-pass filtering, and digitizing the outgoing signal at 500 MSa/s.

III. SQUID FLUX BIASING

Applying an external flux Φ to the SQUID, we can phase bias the JJs such that the phase bias of the junctions is $\phi = \pi\Phi/\Phi_0$ where Φ_0 is the magnetic flux quantum. At half flux ($\Phi/\Phi_0 = 0.5$), the phase of the two junctions is

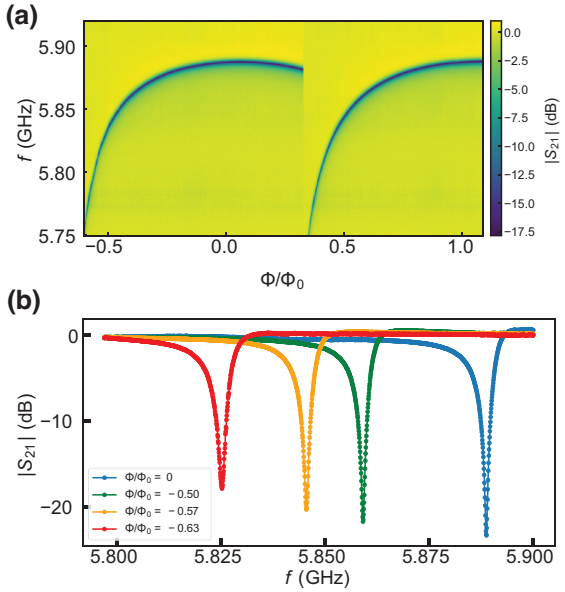

FIG. 2. The flux tuning. (a) The magnitude of the complex transmission $|S_{21}|$ as a function of magnetic flux Φ/Φ_0. (b) The corresponding line cuts.

$\phi = \pi/2$, which, following Eq. (1), creates a maximum Andreev trap of approximately $\Delta_A(\tau = 1)/h \approx 15$ GHz for a superconducting gap $\Delta = 210$ μeV. The CPW SQUID has a resonant frequency of $f_r(\Phi/\Phi_0 = 0.0) = 5.89$ GHz and $f_r(\Phi/\Phi_0 = 0.5) = 5.86$ GHz, corresponding to a Josephson inductance of $L_J(\Phi/\Phi_0 = 0.5) = 0.190$ nH and a critical current of $I_c(\Phi/\Phi_0 = 0.5) = 1.73$ μA (see Appendix E), similar to values reported using dc measurements on Al-InAs heterostructures [57,58]. In Fig. 2(a), we show a color map of the response in $|S_{21}|$ as a function of Φ/Φ_0, where the field is swept from positive to negative magnetic field, with line cuts of the resonance shown in Fig. 2(b). The SQUID response exhibits hysteretic modulation, with f_r continuing to decrease past $\Phi/\Phi_0 = 0.5$. This behavior is typically attributed to a finite loop inductance, as is the case in Ref. [59]. It has been shown in Ref. [60] that the nonsinusoidal CPR of highly transparent junctions can also give rise to a SQUID metapotential that, with increasing flux, develops secondary wells that can trap the fictitious phase particle [40,61,62]. In our device, with each arm of the SQUID loop having an inductance of approximately 30 pH, it is likely a combination of these two effects that leads to the hysteretic and beyond half-flux tunability observed. We provide further details on the SQUID-oscillation periodicity and flux calibration in Appendix D.

Comparing the line cuts in Fig. 2(b), we see that the resonance gets slightly shallower and broader as the applied flux increases. This effect is commonly seen in flux-tuned SQUIDs and can be attributed to a finite subgap resistance in the junctions or to thermal noise [63,64]. We note that

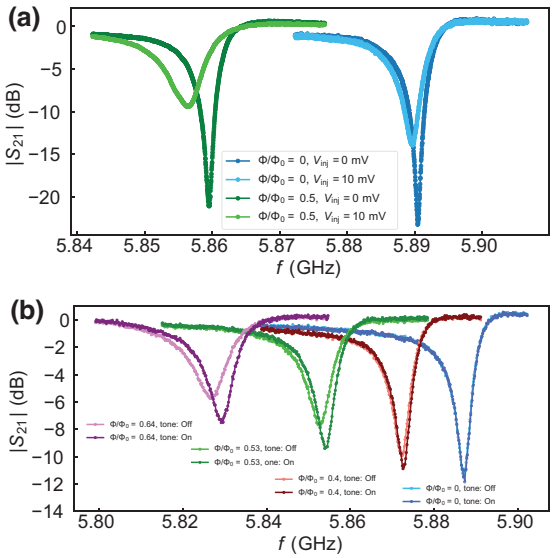

FIG. 3. The effect of QP injection and clearing. (a) Line cuts for zero and half flux at zero and finite injector bias, V_{inj}. The half-flux case shows a more pronounced broadening and frequency shift upon QP injection. (b) Line cuts for different flux values at $V_{\text{inj}} = 10$ mV and photon number = 2, with and without an applied clearing tone of frequency $f_{\text{clear}} = 18$ GHz. The finite-flux cases show the original line shape is somewhat restored with the application of the clearing tone, while the zero-flux case shows no change.

QP trapping in the ABSs result in a similar response to an applied flux. We apply a sufficiently high-frequency clearing tone $f_{\text{clear}} = 18$ GHz on the feed-line input to excite any trapped QPs out of ABS traps. In the presence of QP trapping, we expect the clearing tone to cause the resonance shape to become deeper and narrower as trapped QPs are cleared from the junctions. The frequency $f_{\text{clear}} = 18$ GHz is chosen since it is near the third harmonic of the $\lambda/4$ resonator, where the admittance of the CPW is peaked. Upon the application of the clearing tone, however, we observe no noticeable change to the resonance shape, indicating the absence of QP trapping. This lack of noticeable QP poisoning effects is possibly due to a variety of reasons, which include an insensitivity to single QP poisoning events given our resonance line width and/or a low nonequilibrium QP density near the SQUID; a detailed discussion about this is provided in Appendix E.

We increase the QP density in the circuit by applying a finite voltage bias to the injector junction V_{inj}. As seen in Fig. 3(a), at zero and half flux with $V_{\text{inj}} = 10$ mV the resonance line shape becomes shallower and broader and exhibits a shift toward negative frequency, where the effect is considerably more pronounced in the half-flux case. Two main factors can contribute to this effect: an increase in dissipation due to bulk QP transport in the bulk superconducting film and/or an increase in QP trapping in the ABSs of the junctions in the SQUID. In Fig. 3(b), we plot the resonance curves at $V_{\text{inj}} = 10$ mV with and without an applied clearing tone at different flux biases. The measurements in Fig. 3(b) are performed at a photon number of approximately 2 to avoid any clearing effects from the readout tone f. We observe that at zero flux, the clearing tone does not affect the resonance shape, while at finite flux, the application of the clearing tone results in the resonance becoming sharper and deeper, exhibiting a positive frequency shift, consistent with the clearing of QPs from the ABS traps. These results indicate the presence of QP trapping in ABSs with QP injection when the junctions are phase biased.

IV. QP-INDUCED DEPHASING AND DISSIPATION

By varying the QP density near the junctions, we examine the effects of QPs on the CPW-SQUID device in terms of the internal quality factor Q_{int} and frequency shift Δf_r. We increase the QP density by applying a voltage bias across the injector junction V_{inj} or by raising the temperature T and we also examine the clearing of QPs by the microwave photons of the readout tone. We include measurements of a bare resonator on the same chip as a reference to differentiate between effects resulting from QP trapping in the ABSs of the junctions and from dissipation due to QP transport in the superconducting film. We note that the bare resonator is located 1.6 mm further from the injector junction than the CPW-SQUID device; thus, we expect that at a given V_{inj}, there is a lower density of injected QPs near the bare resonator compared to near the CPW-SQUID device [20]. It is worth mentioning that in the presence of QP trapping in ABSs, changes in Q_{int} are associated more with dephasing of the resonant frequency and the associated frequency noise rather than an increase in dissipative loss [61].

We vary V_{inj} as shown in Fig. 4(a) and find that Q_{int} of the bare resonator decreases due to dissipation from the increased density of QPs in the superconducting Al film. The Q_{int} response of the CPW SQUID at $\Phi/\Phi_0 = 0.0$ and $\Phi/\Phi_0 = 0.5$ shows a pronounced dependence on V_{inj}. While QP-induced dissipation in the resonator of the CPW SQUID is expected to be enhanced due to its position relative to the injector junction, the presence of the junctions can introduce processes such as QP transport via resistive conduction channels in the junction and QP trapping (for the $\Phi/\Phi_0 = 0.5$ case), which can contribute to the pronounced response in Q_{int}. Examining the V_{inj} dependence on the shift in resonant frequency Δf_r presented in Fig. 4(b), we see that the $\Phi/\Phi_0 = 0.5$ case shows a significantly more drastic trend than $\Phi/\Phi_0 = 0.0$. When a high-frequency clearing tone is applied to the $\Phi/\Phi_0 = 0.5$ case, we find that Δf_r shows a significant change, as the shift decreases from 5.7 MHz to 2.1 MHz at $V_{\text{inj}} = 10$ mV, along with Q_{int} increasing by a factor of approximately

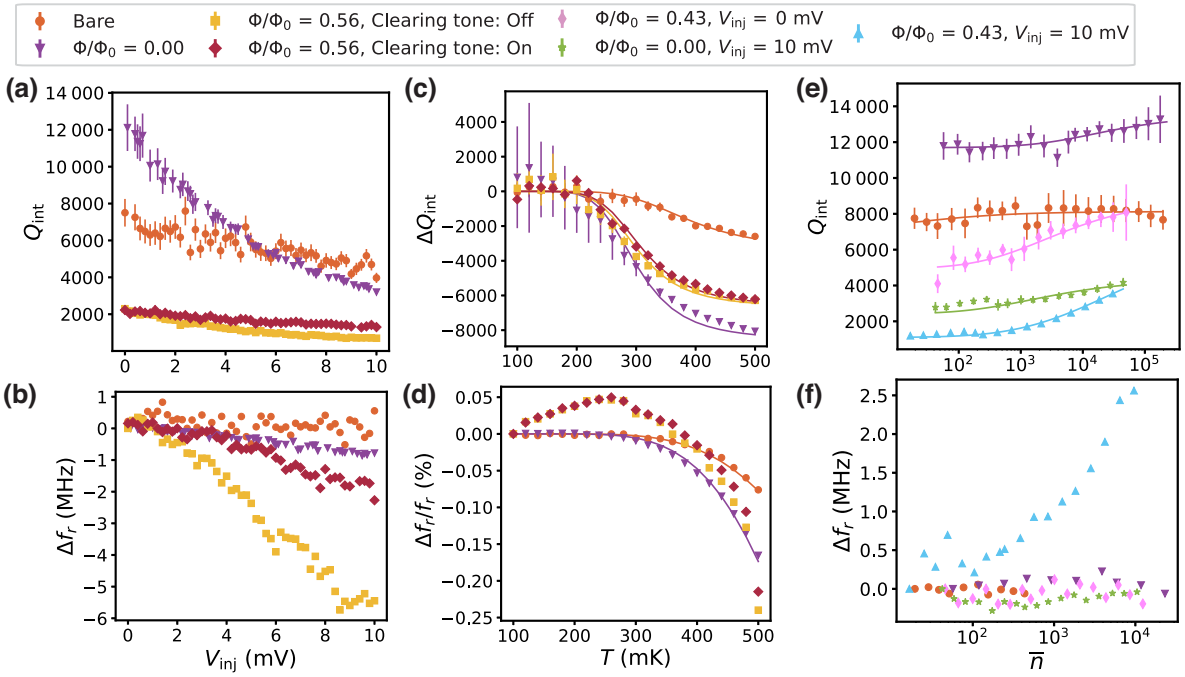

FIG. 4. Microwave loss due to QP effects. The (a),(c),(e) internal quality factor Q_{int} and (b),(d),(f) frequency shift Δf_r as a function of: (a),(b) the voltage bias of the injector junction V_{inj} at $T = 15$ mK, (c),(d) the temperature T without QP injection ($V_{\text{inj}} = 0$ mV) and (e),(f) the photon number $\bar{n}$ at $T = 15$ mK. Δf_r is calculated by subtracting the leftmost f_r value of each data set on the horizontal axis. The solid lines show fits to models for the dependence of Q_{int} on T and $\bar{n}$ and to the dependence of f_r on T.

2. This maximum Δf_r, with the application of the clearing tone, not being closer to the $\Phi/\Phi_0 = 0.0$ case, could indicate inefficiency in the clearing process, as we discuss further in Appendix F. We note that applying a clearing tone to the CPW SQUID at $\Phi/\Phi_0 = 0.0$ does not affect f_r or Q_{int}.

An increase in the equilibrium QP density can also be achieved by increasing the temperature. As we vary the temperature, we observe that Q_{int} is roughly unchanged until $T \approx 200$ mK for the CPW SQUID and $T \approx 300$ mK for the bare resonator, at which point Q_{int} starts to decrease, as shown in Fig. 4(c). The dependence is again seen to be more pronounced in the CPW SQUID than the bare resonator. To analyze the trend in Q_{int}, it is useful to write the total Q_{int} as an inverse sum of terms that capture the temperature T and photon-number $\bar{n}$ dependencies separately, being

$$\frac{1}{Q_{\text{int}}(T,\bar{n})} = \frac{1}{Q_0} + \frac{1}{Q(T)} + \frac{1}{Q(\bar{n})}, \tag{2}$$

where Q_0 describes losses independent of T and $\bar{n}$. These terms can be interpreted as contributions to loss due to thermal QPs, in the case of $Q(T)$, and QP excitation due to the readout tone, $Q(\bar{n})$. We consider a model for the temperature-dependent surface impedance following the Mattis-Bardeen theory, where the temperature-dependent internal quality factor is given by

$$Q(T) = Q_{\text{QP},0} \frac{e^{\Delta/k_B T}}{\sinh\left(\frac{hf_r}{2k_B T}\right) K_0\left(\frac{hf_r}{2k_B T}\right)}, \tag{3}$$

as described in Refs. [65,66], where $Q_{\text{QP},0}$ is the inverse linear absorption by QPs and $\Delta = 210$ μeV is the superconducting gap of aluminum. The resonant frequency f_r is set to the value at $T = 100$ mK. The only free parameters in the fit are $Q_{\text{QP},0}$ and the inverse sum $1/Q_0 + 1/Q(\bar{n})$. The fit to Eq. (3) for each data set is shown in Fig. 4(c). Here, we plot the results in terms of the change in internal quality factor ΔQ_{int} to accentuate the temperature dependence. For the bare resonator, we find that the inverse linear absorption for the bare resonator is $Q_{\text{QP},0} = 3.74$. This benchmarks QP dissipation due to the superconducting Al film in the resonator. We find that in the CPW-SQUID device, at $\Phi/\Phi_0 = 0.0$, $Q_{\text{QP},0}$ decreases to 1.28, lower than that of the bare resonator by 66%. This implies that other temperature-dependent factors play a role with the addition of the SQUID loop to the resonator, such as the critical current carried by the junctions, the number of resistive channels, and the induced superconducting gap of the junctions. Further, we find that as the SQUID is flux biased to $\Phi/\Phi_0 = 0.5$, $Q_{\text{QP},0}$ further decreases to 1.02. This decrease is expected and corresponds to the effect of QP trapping. An interesting observation is the recovery of

$Q_{QP,0}$ upon the application of a clearing tone, where $Q_{QP,0} = 1.27$, which is almost the value of $Q_{QP,0}$ for $\Phi/\Phi_0 = 0.0$. Shifting our focus to the Δf_r dependence, presented in Fig. 4(d), the $\Phi/\Phi_0 = 0.5$ case shows a gradual increase in Δf_r up until $T \approx 250$ mK, rather than staying constant like the bare resonator and the CPW SQUID at $\Phi/\Phi_0 = 0.0$. This increase in frequency with temperature is consistent with the suppression of QP trapping due to the growing population of thermal phonons, as observed in Ref. [67], with hotter QPs being less likely to relax and get trapped in lower-energy trap states or an increase in QP clearing mediated by phonon absorption [47,49]. While the equilibrium phonons do not provide enough energy (approximately 5.2 GHz at $T = 250$ mK) for the QPs to be cleared from the deepest Andreev traps directly to the continuum, the presence of intermediate transparency modes as seen in Fig. 1 and mode-to-mode coupling [46] can also support excitations of QPs from deep high-transparency modes to shallower modes with less transparency and eventually to the continuum through multiple transitions. At temperatures above 250 mK, the effect of the rising QP density dominates and Δf_r begins to decrease in a similar fashion to the bare resonator and SQUID with $\Phi/\Phi_0 = 0.0$. In Fig. 4(d), we also show fits to the Mattis-Bardeen theory for the change in frequency as a function of temperature for the bare resonator and CPW SQUID at zero flux, where the data are seen to fit well (for further details, see Appendix G). On the other hand, the half-flux case does not fit well to the Mattis-Bardeen model, mainly due to the thermal excitation and trapping of QPs.

We next consider the dependence of Q_{int} and Δf_r on the photon number $\bar{n}$ of the readout tone, presented in Figs. 4(e) and 4(f). The bare resonator shows a Q_{int} that is approximately independent of $\bar{n}$, suggesting that the loss is not limited by two-level systems (TLSs) [66,68,69]. At $V_{\text{inj}} = 0$ mV, a similar $\bar{n}$-independent loss is observed in the CPW SQUID at $\Phi/\Phi_0 = 0.0$ but not at $\Phi/\Phi_0 = 0.5$. The $\bar{n}$ dependence observed is more pronounced at $V_{\text{inj}} = 10$ mV for $\Phi/\Phi_0 = 0.5$. This $\bar{n}$ dependent pattern is also seen in Δf_r for the $\Phi/\Phi_0 = 0.5$ case at $V_{\text{inj}} = 10$ mV, where Δf_r decreases by 2.5 MHz from high to low $\bar{n}$. These results are consistent with the clearing of trapped QPs mediated by the photons of the readout tone. Similar to clearing mediated by thermal phonons, the absorption of microwave photons, and even photons that carry less energy than the Andreev depth ($f = 5.86 - 5.89$ GHz compared to $\Delta_A(\tau = 1)/h \approx 15$ GHz), can contribute to the clearing of QPs through multiphoton transitions and excitations to subsequently higher-energy Andreev levels at high enough $\bar{n}$, as is evident from Fig. 4(f). On the other hand, at low $\bar{n}$, the readout tone does not provide enough power to support QP clearing from the ABSs, leading to a saturation in the low-power frequency shift and internal quality factor. This suggests that, at low temperatures, electron-photon interactions can be a contributing mechanism to QP clearing, consistent with results reported for Al-nanobridge junctions [49].

We consider the changes in Q_{int} as a function of photon number to be associated with the changing densities of trapped and mobile QPs via excitation to the continuum via the readout tone. It has been shown in Ref. [70] that one can write a phenomenological model to describe the changing densities of localized QPs (x_l) and mobile QPs (x_m). By using a set of coupled equations, one can determine the power dependence of the loss, $1/Q_{\text{int}}$, in terms of the density of localized QPs. While the model considers the rates of QP recombination, excitation, localization, and generation, it is assumed that only QP excitation is power dependent, proportional to the number of photons through $\Gamma_{\text{ex}} = \Gamma_0 \bar{n}$, where Γ_{ex} is the rate of QP excitation and Γ_0 characterizes the photon-QP coupling strength. Assuming that the density of states of trapped QPs is much greater than that of mobile QPs, one can write the power-dependent loss $1/Q(\bar{n})$ as a function proportional to only the density of localized QPs x_l. By solving for the steady-state solutions of these equations along with further simplifying assumptions (see Appendix H), the power-dependent loss due to localized QPs can be written as

$$Q(\bar{n}) = \frac{1}{\beta}\left[1 + \frac{\gamma\bar{n}}{1 + \frac{1}{2}(\sqrt{1 + 4\gamma\bar{n}} - 1)}\right]. \tag{4}$$

Here, the prefactor β is proportional to the density of localized QPs, proportional to the ratio of QP localization and recombination of mobile and localized QPs $\Gamma_{\text{loc}}/\Gamma_{\text{ml}}$. The factor γ is defined as $\gamma = 2\Gamma_{\text{loc}}\Gamma_0/g_m\Gamma_{\text{ml}}$, where g_m is the generation rate of mobile QPs. Fitting the data for Q_{int} to Eq. (4), we find that the bare resonator has $\beta = 1.80 \times 10^{-5}$, while in the CPW-SQUID device, $\beta = 1.08 \times 10^{-5}$ at $\Phi/\Phi_0 = 0.0$. We find that β increases to 9.01×10^{-5} at $\Phi/\Phi_0 = 0.5$. If we assume that the rate for QP recombination is independent of the applied flux, this corresponds to the increase in the rate of QP localization at $\Phi/\Phi_0 = 0.5$ of a factor of 15, which we expect to be due to the deepening of the ABS traps with applied flux. With QP injection at $V_{\text{inj}} = 10$ mV, we find that β increases to $\beta = 1.86 \times 10^{-4}$ at $\Phi/\Phi_0 = 0.0$ and to $\beta = 7.47 \times 10^{-4}$ at $\Phi/\Phi_0 = 0.5$ compared to without QP injection. These results imply that the QP-localization rate increases with an applied finite V_{inj}, increasing the background QP density. We also anticipate that by increasing the number of mobile and trapped QPs, the rate of recombination should increase as well, possibly explaining why the increase in β for the SQUID with $\Phi/\Phi_0 = 0.5$ is not as drastic as that for the $\Phi/\Phi_0 = 0.0$ case. In terms of fitting for γ, we find that several different values for γ yield similar fit results. The value of γ used to obtain the fits for the bare resonator is 0.013, that for the SQUID with $\Phi/\Phi_0 = 0.0$ is 0.002, and that for the SQUID with $\Phi/\Phi_0 = 0.5$ is 0.001.

V. TRAPPING AND CLEARING DYNAMICS

In order to further probe the dynamics of QP trapping and clearing, we monitor the response of the resonance in time while pulsing a clearing tone. The protocol used is shown in Fig. 5(a): a constant V_{inj} is applied, constantly injecting QPs into the system and resulting in a finite population of QPs occupying the trap states. An applied high-frequency clearing tone $f_{\text{clear}} = 18$ GHz is mixed with a 100-μs-wide square pulse output by an arbitrary wave form generator with a sampling rate of 1 GSa/s. The two quadratures of the output signal, I and Q, are measured as the clearing tone is pulsed and is averaged over 10 000 runs. Figure 5(b) shows an example of the response of I measured in time, where a decay is observed when the pulse begins ($t = 200$ μs), corresponding to a shift in the resonant frequency upon the application of the clearing tone and the clearing of QPs. The resonance reaches a steady state with the clearing tone applied and when the clearing-tone pulse ends ($t = 300$ μs), I decays to its initial values as QPs start to reoccupy the traps. We fit the quadrature responses at the start and end of the pulse in time to an exponential decay and extract two time constants: the clearing time and the trapping time. The clearing time t_{clear} is the time constant associated with the excitation of QPs from the Andreev traps mediated by the applied clearing tone, while the trapping time t_{trap} is the time constant associated with the relaxation of QPs from the continuum into the Andreev traps once the pulse ends. If the clearing and trapping events are uncorrelated, the clearing and trapping times correspond to the rate for individual QPs to clear or get trapped.

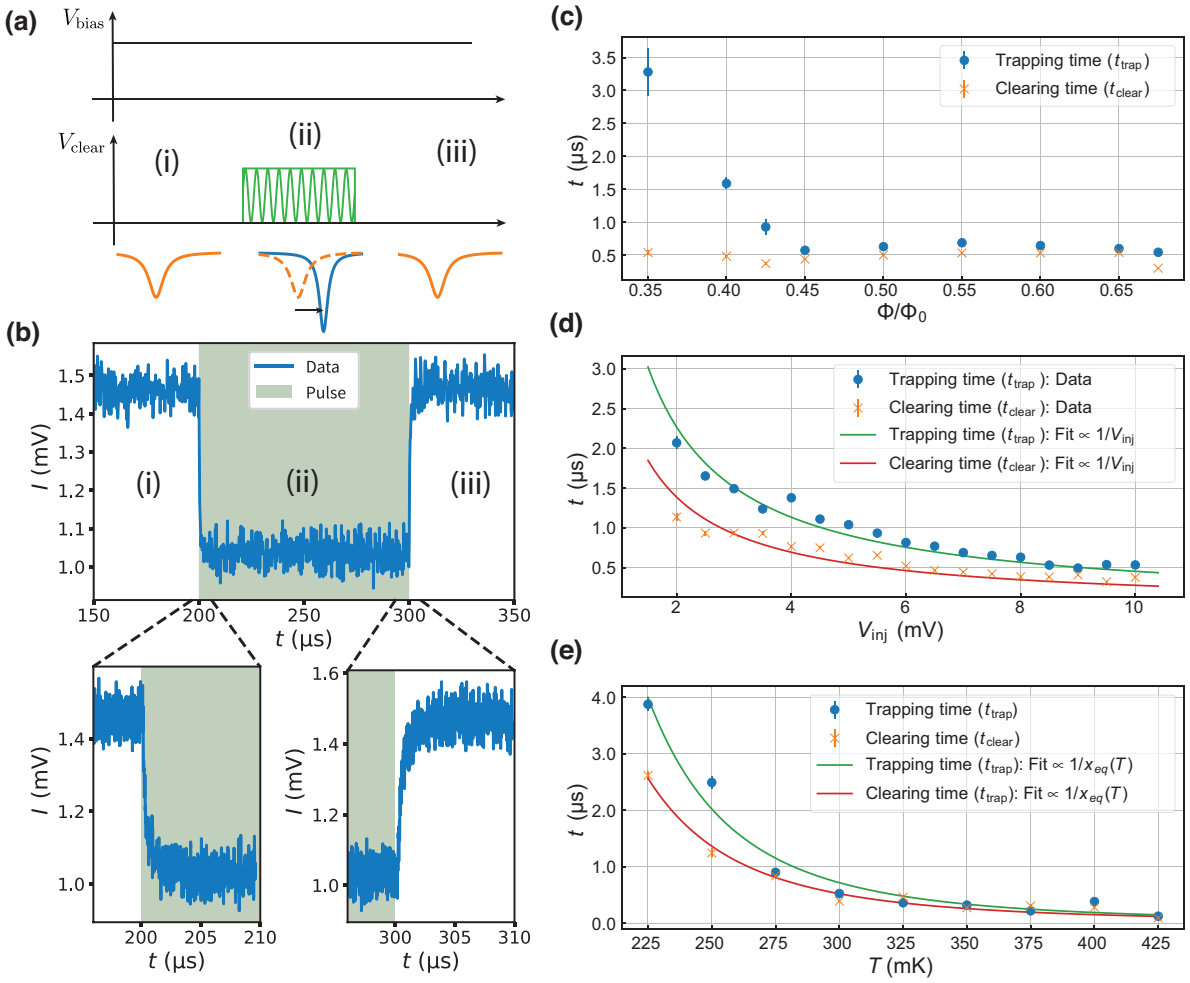

FIG. 5. QP trapping and clearing. (a) The protocol for QP clearing. (i) While the in-phase (I) and quadrature (Q) components are measured, a constant $V_{\text{inj}} = 10$ mV being applied such that a finite QP density populates the trap states. (ii) A 100-μs-long clearing-tone pulse with $f_{\text{clear}} = 18$ GHz is applied, which clears out the QPs. (iii) The clearing-tone pulse ends and QPs fall back into the trap states. (b) An example measurement of the I response over time t. The region where the clearing-tone pulse is on is shaded in green. The clearing time t_{clear} and the trapping t_{trap} are extracted from an exponential fit of the I or Q response to the start (bottom left plot) and end of the pulse (bottom right plot), respectively. (c)–(e) The trapping and clearing times as a function of Φ/Φ_0, V_{inj}, and the temperature T, respectively: (c) $V_{\text{inj}} = 10$ mV, $T = 15$ mK; (d) $\Phi/\Phi_0 = 0.49$, $T = 15$ mK; (e) $\Phi/\Phi_0 = 0.49$, $V_{\text{inj}} = 0$ mV.

We first tune the trap depth Δ_A via flux Φ/Φ_0 and monitor the effect on t_{trap} and t_{clear} at $V_{\text{inj}} = 10$ mV, as seen in Fig. 5(c). Between $\Phi/\Phi_0 = 0.35$ and 0.675, we find trapping times of order 1 μs, which decrease as a function of Φ/Φ_0. The trend implies that deeper Andreev traps are more likely to trap QPs, consistent with the electron-phonon relaxation mechanism for QP trapping [20,47,49]. We note that the time scale set by coupling to the resonator is approximately 27 ns.

On the other hand, the clearing time is expected to be less dependent on flux and should depend on the clearing-tone power [47]. This is because the clearing tone should provide sufficient energy to excite QPs out of the deepest Andreev traps—if not directly to the continuum, then to lower-transparency modes carrying significantly less supercurrent and correspondingly contribute less to the response. This is consistent with the data in Fig. 5(c), where t_{clear} remains around approximately 500 ns at all fluxes. We note that below $\Phi/\Phi_0 = 0.35$, the signal-to-noise ratio is too low to obtain an accurate fit. The fact that the clearing and trapping times are of similar magnitudes might also contribute to the inefficiency of the clearing tone, as discussed for the Δf_r results shown in Fig. 4(b), where Andreev states can remain partially occupied in the presence of the clearing tone as the system reaches a steady state where trapping and clearing events balance, providing a finite QP occupation probability even in the presence of the clearing tone.

Assuming that QP trapping and clearing are independent processes and that the clearing tone can be treated as a large bath of photons, such systems are typically described by a Markovian model [49]. In this case, the trapping and clearing rates of individual QPs are expected to be independent of the QP density. In Fig. 5(d), we present the dependence of t_{trap} and t_{clear} on V_{inj} at $\Phi/\Phi_0 = 0.49$. Without QP injection and up to $V_{\text{inj}} = 2$ mV, we do not observe a noticeable trapping or clearing response in I or Q (see Appendix I). Above $V_{\text{inj}} = 2$ mV, we find that as the QP density increases, t_{trap} decreases by a factor of 4 at $V_{\text{inj}} = 10$ mV. This corresponds to the system recovering to a steady state faster, suggesting faster trapping rates when the QP density is higher. The QP-density-dependent trapping rates can be attributed to a rise in phonon populations at higher QP densities. An increase in QP recombination at higher QP densities results in the emission of high-energy ($\geq 2\Delta_0$) phonons, which can then enhance the number of stimulated-emission events for QPs and consequently help increase the QP relaxation and trapping rates, decreasing the trapping times. Further, QP relaxation mediated by phonon emission, typically low-energy phonons, can also contribute to the increasing phonon population and, consequently to the increase in trapping rates. Interestingly, t_{clear} also exhibits a dependence on V_{inj} decreasing by a factor of 3 in the measured V_{inj} range. This t_{clear} dependence implies that QPs are more likely to be cleared out of the Andreev traps at higher QP densities. This is possibly also due to the rise in phonon populations, generated through QP recombination and phonon-mediated QP relaxation, that can then participate in the excitation of QPs out of the deepest Andreev traps either directly to the continuum or through multiple transitions, increasing the clearing rate, which corresponds to a decrease in the clearing times. These results suggest that electron-phonon interactions can play a considerable role in QP dynamics even at low temperatures. Further, we find that both t_{trap} and t_{clear} fit inversely proportionally to V_{inj} as shown with the fits in Fig. 5(d). The origin of this dependence can be understood by considering a phenomenological model for the QP density as discussed in Appendix J.

Finally, we examine the effect of raising the temperature T without QP injection ($V_{\text{inj}} = 0$ mV), corresponding to increasing the thermal equilibrium QP density x_{eq}, which varies as

$$x_{\text{eq}}(T) = \sqrt{\frac{2\pi k_B T}{\Delta}} \exp\left(\frac{-\Delta}{k_B T}\right), \tag{5}$$

where k_B is Boltzmann's constant and Δ is the superconducting gap. Below $T = 225$ mK, we are unable to accurately read out an exponential decay in I and Q due to the low QP density (see Appendix I). Starting $T = 225$ mK, we observe the t_{trap} and t_{clear} decay as a function of T as seen in Fig. 5(e), reaching values of a few hundreds of nanoseconds. The trends observed in Fig. 5(e) as a function of T are similar to that of Fig. 5(d). Here, the suppression of t_{trap} and t_{clear} can also be attributed to the increasing recombination rate with increasing thermal QP density as well as to the increased phonon population at higher temperatures and phonon emission generated by QP recombination and QP inelastic scattering. As with the V_{inj} case, the recombination and excitation of trapped QPs through phonon absorption are responsible for the decrease of t_{clear} with T. Another contributing factor is the suppression of the induced gap at higher temperatures, resulting in the Andreev traps getting shallower. By fitting the temperature dependence of t_{trap} and t_{clear}, we find that both fit well to $1/x_{\text{eq}}(T)$ if the superconducting gap is reduced by a factor of 1.5, as seen in the fits shown in Fig. 5(e). The inverse dependence of t_{trap} and t_{clear} on T can be understood by considering a phenomenological model for the QP density as described in Appendix J; however, further investigation is required to understand the origin of such superconducting-gap suppression. The observed trends in trapping and clearing times as a function of V_{inj} and T suggest that our system is not well described by a simple Markovian model; rather, the QP dynamics observed in such planar junctions fabricated on hybrid superconductor-semiconductor structures involve

interdependent mechanisms and warrants further theoretical understanding. Future work can explore to what degree these systems act as Markovian or non-Markovian.

VI. CONCLUSIONS

In conclusion, we have studied QP-induced losses as well as QP trapping and clearing dynamics in high-transparency Al-InAs planar JJs. By examining the resonance line shape as a function of local QP injection, temperature, and photon number, we have observed lineshape broadening and frequency shifts consistent with QP trapping. Using a model for the excitation of trapped QPs, we have found a factor-of-15 increase in the QP trapping rate as we flux bias the SQUID from 0.0 to 0.5 flux, corresponding to trapping in the deepened ABSs. By performing time-domain measurements, we have observed that the trapping and clearing rates occur on a time scale that varies from a few microseconds to hundreds of nanoseconds, depending on the trap depth and QP density. The results indicate that the relaxation of QPs relies on electron-phonon interactions. On the other hand, the excitation mechanisms of QP from the traps are observed to have contributions from microwave photons and phonon absorption. The trapping and clearing times depending on the QP density suggest the presence of phonon-mediated QP-QP interactions in the system. The results highlight the trapping and clearing dynamics of QPs in a hybrid superconductor-semiconductor platform and the resulting effects on microwave loss. The time scales for QP trapping reported here are relevant in developing topological and superconducting qubits on hybrid superconductor-semiconductor systems.

ACKNOWLEDGMENTS

We thank Max Hays and Enrico Rossi for fruitful discussions. The NYU team acknowledge support from the Army Research Office Agreements No. W911NF2110303 and No. W911NF2210048. The NYU team also acknowledge support from Multidisciplinary University Research Initiative (MURI) Office of Naval Research (ONR) Award No. N00014-22-1-2764 P00001 and from the National Science Foundation (NSF) Agreement No. 2340-206-2014878 A01. W.M.S. acknowledges funding from the Army Research Office (ARO)–Laboratory for Physical Science (LPS) Quantum Computing Research (QuaCR) Graduate Fellowship Agreement No. W911NF2110303. The USC team acknowledge support from the Air Force Office of Scientific Research (AFOSR) under Award No. FA9550-19-1-0060 and from the NSF under Award No. DMR-1900135. We acknowledge the MIT Lincoln Laboratory and the Intelligence Advanced Research Projects Activity (IARPA) for providing the traveling-wave parametric amplifier used in this work. We thank Søren Anderson for providing the schematics shown in Fig. 10.

APPENDIX A: TIGHT-BINDING CALCULATIONS

We conduct tight-binding simulations using the KWANT PYTHON package [71] along the lines of the work presented in Ref. [72]. The simulation considers a two-dimensional (2D) system where a semiconductor region separates two superconducting leads. The system is described by the Hamiltonian

$$\begin{bmatrix} H & \Delta(x) \\ \Delta(x)^* & -H \end{bmatrix}, \quad H = -\frac{\hbar^2}{2m^*}\nabla^2 - \mu, \tag{A1}$$

where m^* is the effective electron mass, and μ is the chemical potential. The superconducting pairing potential $\Delta(x)$ varies spatially as

$$\Delta(x) = \begin{cases} \Delta_0, & \text{if } x < -l/2, \\ 0, & -l/2 < x < l/2, \\ \Delta_0 e^{i\phi}, & \text{if } x > l/2, \end{cases} \tag{A2}$$

where Δ_0 is the superconducting gap, l is the junction length, and ϕ is the phase difference across the two superconducting leads. We discretize the above Hamiltonian on a square lattice with lattice constant $a = 5$ nm and simulate a system with $w = 1$ μm, normal region length $l = 100$ nm, geometrical length of the superconductor $l_{sc} = 2$ μm (which is larger than the coherence length of the proximitized 2DEG $\xi = 1373$ nm calculated using $\xi = \hbar\sqrt{2\mu/m^*}/\Delta$ using the following parameters), superconducting gap $\Delta_0 = 210$ μeV, carrier density $n = 4 \times 10^{11}$ cm^{-2}, effective electron mass $m^* = 0.04m_e$, and electron mass m_e. To calculate the Andreev spectrum, we diagonalize the Hamiltonian and plot the energy as a function of ϕ.

APPENDIX B: MATERIAL GROWTH AND DEVICE FABRICATION

The CPW-SQUID devices are fabricated on an InAs near-surface quantum well grown by molecular-beam epitaxy on a 500-μm-thick InP substrate. After thermal oxide desorption, an $In_xAl_{1-x}As$ graded buffer layer is grown to reduce strain on the InAs active region, where the composition x is graded from 0.52 to 0.81. The InAs 2DEG is confined to $In_{0.81}Ga_{0.19}As$ top and bottom barriers. Finally, a 30-nm film of Al is deposited *in situ*. The procedure for the growth of the III-V heterostructure is outlined in Refs. [50,51,53].

The design is constructed using QISKIT METAL [73] and rendered in the ANSYS high-frequency simulation software (HFSS) [74] to simulate the expected resonant frequency, external quality factors, and electromagnetic field distribution. The chip design consists of four hanger CPW resonators coupled to a transmission line, as seen in Fig. 6. The external quality factor is designed to be $Q_{ext} \sim 1500$.

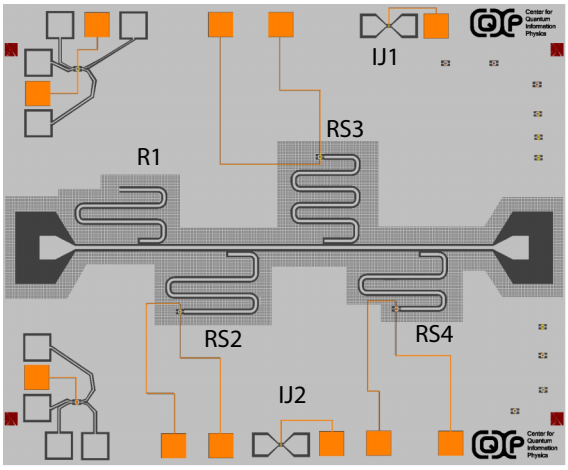

FIG. 6. A schematic of the chip design. The chip has three $\lambda/4$ CPWs shunted to ground through a SQUID loop (RS2, RS3, and RS4) and one bare resonator (R1). The design also includes two injector junctions (IJ1 and IJ2). In this work, we focus on RS3, R1, and IJ1.

Three $\lambda/4$ CPWs are shunted to ground through a SQUID loop with two geometrically symmetric JJs. These devices are called CPW SQUIDs (RS2, RS3, and RS4). One bare CPW (R1), which does not have a SQUID loop and is shorted to ground directly, is used as a reference. We also add two two-terminal JJs as "injector" junctions (IJ1 and IJ2) to inject QPs into the circuit. The injector junction is equipped with a gate, as shown in Fig. 1(f), that is kept grounded during the measurements. In this work, we focus on RS3, R1, and IJ1.

The device is fabricated with electron-beam lithography steps using spin-coated PMMA resist. First, we define the microwave circuit and chemically etch the Al using Transene Al etchant type D and the III-V layers using an III-V etchant consisting of phosphoric acid (H_3PO_4, 85%), hydrogen peroxide (H_2O_2, 30%), and deionized water, in a volumetric ratio of 1:1:40. The junctions in the CPW SQUID are defined to be approximately 4 μm and the injector junction to be approximately 8μm. The planar junction is then defined by etching a thin 100-nm strip of Al. Considering an electron mean free path of approximately 200 nm as measured by low-temperature Hall measurements, the junction should be in the short ballistic regime. Around the microwave circuit, we also etch 2×2 μm holes in the Al ground plane that are 10 μm apart to act as flux-pinning holes. We then blanket deposit a 40-nm layer of AlO_x as a gate dielectric by atomic layer deposition, followed by a sputtered gate electrode made of a 50-nm Al layer using lift-off. In all measurements, the gates are kept grounded. A schematic of the junction heterostructure after fabrication is shown in Fig. 7.

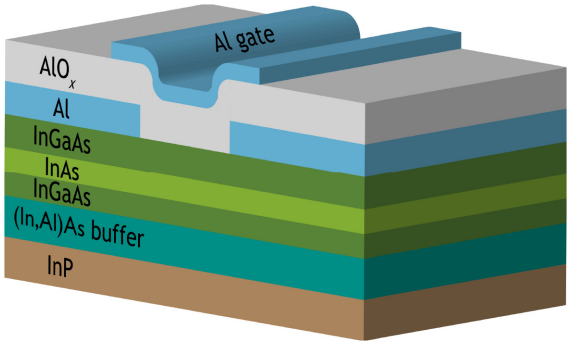

FIG. 7. A schematic of the material heterostructure with a junction, made of Al superconducting contacts and an InAs surface quantum well. A layer of AlO_x is deposited as a gate dielectric, followed by a patterned Al gate.

APPENDIX C: MEASUREMENT SETUP

A schematic of the measurement setup is shown in Fig. 8. The measurements are conducted in an Oxford Triton dilution refrigerator. The sample is embedded in a QCage, a microwave sample holder, and connected to the printed circuit board by aluminum wire bonds. Probe signals are sent from a vector network analyzer or a microwave signal generator and attenuated by −56 dB, with attenuation at each plate as noted. The signal then passes through a (1–18)-GHz band-pass filter made of a copper box filled with cured Eccosorb castable epoxy resin. The signal is sent through the sample, returned through another Eccosorb filter, and passed through an isolator with 20 dB isolation and 0.2 dB insertion loss. The signal is then amplified by a traveling-wave parametric amplifier, passed through another isolator, and then amplified with a low-noise amplifier mounted to the 4 K plate and two room-temperature amplifiers (MITEQ) outside the refrigerator.

We utilize the injector junction to increase the QP density of the system by voltage biasing it above twice the superconducting gap. The two-terminal JJ is biased by grounding one terminal and applying a voltage bias to the other terminal. As mentioned in the main text, all the dc lines in the refrigerator go through a QDevil QFilter, a low-pass filter that is mounted on the mixing chamber. The filters add a resistance of 1.7 kΩ to each dc line. Our reported applied voltage bias values to the injector junction V_{inj} is applied across the filter and the injector junction in series. Given that the normal resistance of the injector junction is unknown, it is difficult to determine the actual value of the voltage applied to or the power dissipated by the injector junction. However, we can make a simple approximation by noting that the data in Fig. 4 and the fact that no noticeable jumps in I and Q are observed when applying the clearing tone below $V_{\mathrm{inj}} = 2$ mV, imply that considerable QP injection starts around $V_{\mathrm{inj}} = 2$ mV.

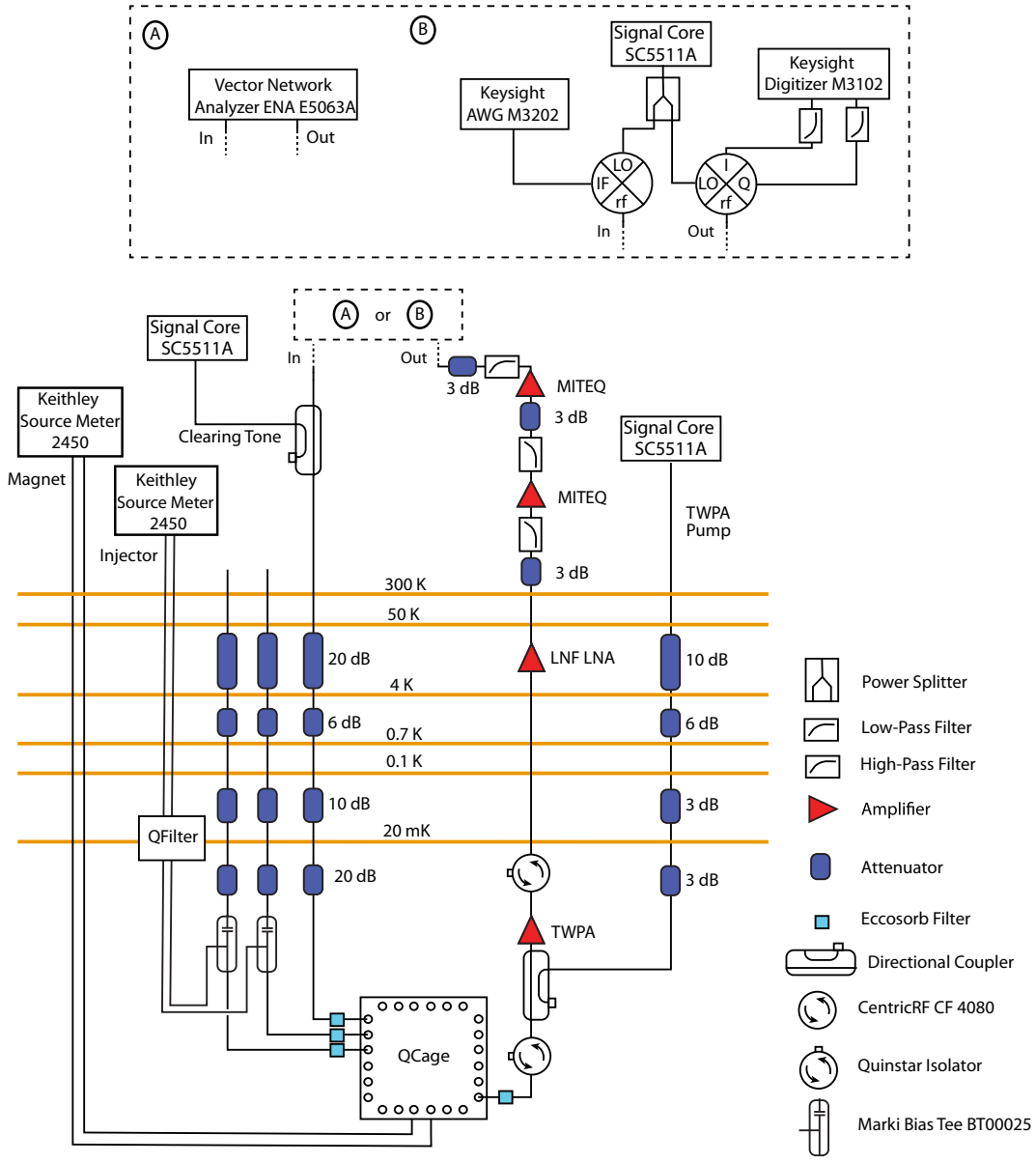

FIG. 8. A schematic of the cryogenic and room-temperature measurement setup.

This would correspond to the actual voltage bias reaching the injector junction being around $2\Delta_0 \sim 440$ μeV at $V_{\text{inj}} = 2$ mV. In that case, the normal resistance of the injector junction would be approximately 375Ω, which is similar to what has been reported in other works on Al-InAs junctions with similar geometries [42,45]. We note that while we estimate 2Δ corresponding to $V_{\text{inj}} = 2$ mV, we do not see an obvious jump in the data that would signal the start of QP injection at this voltage bias, suggesting that there may be finite dissipation at all voltage biases.

APPENDIX D: FLUX CALIBRATION

For the CPW-SQUID device, the SQUID is expected to show a periodic dependence as a function of Φ, with periodicity Φ_0, which should be reflected in the resonant frequency of the resonator. To extract the periodicity of the SQUID oscillations and calibrate the x axis from the out-of-plane magnetic field $B_\perp$ to Φ/Φ_0 as shown in Fig. 2(a), we first extract the resonant frequency of the data presented. The extracted resonant frequencies of the oscillations in Fig. 2(a) are shown in Fig. 9(a) as a function of $B_\perp$. We then find the $B_\perp$ point corresponding to the maximum frequency for each of the two oscillations and the difference in $B_\perp$ between these two points $\Delta B_\perp = 3.25$ μT is considered to be the periodicity of the SQUID oscillations. To calibrate the x axis from $B_\perp$ to Φ/Φ_0 as shown in Fig. 2(a), we subtract the value of $B_\perp$ for the maximum frequency of the left oscillation and divide the axis by $\Delta B_\perp$.

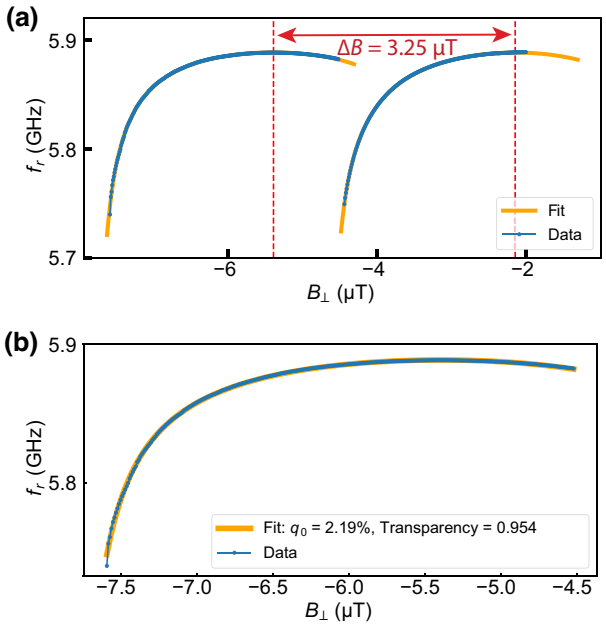

FIG. 9. (a) The extracted resonant frequencies f_r from Fig. 2(a) as a function of the out-of-plane magnetic field $B_\perp$. The periodicity of the oscillations is found by finding the $B_\perp$ values at the maximum of each oscillation. (b) The extracted resonant frequencies and fit for the SQUID oscillation using Eq. (D1).

We fit the SQUID oscillations shown in Fig. 9(a) to extract details of the SQUID device. Similar to the approaches taken in Refs. [48,60], the resonant frequency can be described by

$$\omega(\phi) = \omega(0)\left[1 + q_0 \frac{L_J(\phi) - L_J(0)}{L_J(0)}\right]^{-1/2}, \qquad \text{(D1)}$$

with

$$I_{\mathrm{ABS}}(\phi) = \frac{e\Delta_0}{2\hbar} \frac{\tau \sin(\phi)}{\sqrt{1 - \tau \sin(\phi/2)}}, \qquad \text{(D2)}$$

where $q_0 = L_J(0)/(L_0 + L_J(0))$ is the participation ratio and $\Delta_0 = 210\ \mu\mathrm{eV}$ is the superconducting gap. Fitting the left SQUID oscillation to Eq. (D1), as presented in Fig. 9(b), results in periodicity $\Delta B_\perp = 3.4\ \mu\mathrm{T}$ with a participation ratio of $q_0 = 2.19\%$ and transparency $\tau = 0.954$, as seen in Fig. 9(b). This $\Delta B_\perp$ value is close to what is determined from Fig. 9(a) by comparing the maximum-frequency points of two oscillations.

APPENDIX E: NONEQUILIBRIUM QP DENSITY

As discussed in the main text, without QP injection, i.e., $V_{\mathrm{inj}} = 0$ mV, and at low temperature, we do not observe a QP clearing effect with the application of the clearing tone. We also confirm that with time-domain measurements, we are unable to see jumps between QP occupation states corresponding to QP poisoning events in real time, as has been observed in Refs. [31,48]. Several factors may contribute to this, which include a low sensitivity to QP poisoning and a low QP density near the SQUID.

1. Sensitivity to QP poisoning

For the CPW SQUID, the junctions add a total inductance $L_J/2$ in series to the CPW, where L_J is the inductance of each junction. The measured resonant frequency of the CPW-SQUID device is therefore determined by L_0, L_J, and the kinetic inductance of the thin Al film, L_K. We use a bare resonator on the same chip to estimate L_K of the thin-film Al superconductor. For the bare resonator, we calculate the kinetic inductance fraction $\alpha_K = 1 - (f_r/f_0)^2 = 7.27\%$, where f_r and f_0 are the measured and geometric resonant frequencies, respectively. This sizable kinetic inductance is expected for the thin epitaxial Al film. The L_K of the CPW SQUID is then given by $L_0\alpha_K$, where L_0 is determined using an analytical expression for the inductance of a $\lambda/4$ CPW using conformal-mapping techniques [75]. By knowing the values of L_0, L_K and f_r one can uniquely determine the value of L_J in the CPW-SQUID device, as described further in Ref. [39].

At $\Phi/\Phi_0 = 0.5$, the CPW-SQUID device has a resonant frequency of $f_r = 5.860$ GHz and a line width of 8.455 MHz. This corresponds to a Josephson inductance of $L_J(\Phi/\Phi_0 = 0.5) = 0.190$ nH and a critical current of $I_c(\Phi/\Phi_0 = 0.5) = 1.73\ \mu\mathrm{A}$. Semiclassically, we can estimate the number of modes to be $N_e \sim w/\lambda_F \approx 280$, where λ_F is the Fermi wavelength. Thus, the average current carried by a single mode is $I_c/N_e = 6.19$ nA and a corresponding single QP poisoning event would result in a frequency shift of approximately 0.28 MHz on average. In practice, we expect deeper traps to have a higher chance of occupying QPs (assuming electron-phonon interactions, the rate of QP trapping can be taken to be $\propto \Delta_A^3$ [49,76,77] near Δ_0 by solving the kinetic equation for a QP distribution) and the supercurrent to be carried mainly by high-transparency modes as implied by Fig. 1(b). For a mode in the ballistic limit carrying the maximal current ($\tau = 1$) of $e\Delta/\hbar \approx 51$ nA, a QP poisoning event results in a shift of approximately 2.46 MHz. Thus, due to the wide distribution of transparencies, we expect QP poisoning events to result in a frequency shift between these two values per trapped QP. Given our signal-to-noise ratio, it could be the case that shifts due to QP trapping are considerably less than the line width of the resonance. Consequently, without QP injection and at low temperatures, the number of trapped QPs would not result in a significant effect on the resonance shape when the clearing tone is applied or allow us to observe single QP trapping in real time given the sensitivity to QP trapping. On the other hand, with QP injection and at higher temperatures, the QP

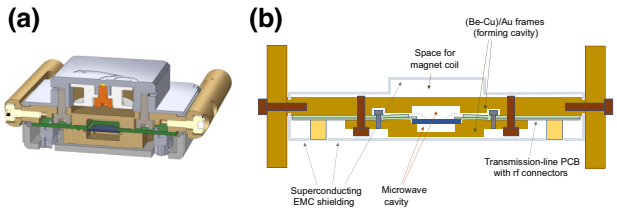

FIG. 10. (a) A three-dimensional diagram of the QCage sample holder. (b) A cross-section view of the sample holder showing the Au-plated (Be-Cu) frames that create the inner cavity and the superconducting shielding.

density is high enough that a sufficient amount of QPs are trapped such that the application of the clearing tone has a noticeable effect on the resonance shape.

2. Possible low QP density near the junctions

In addition to the low sensitivity to QP trapping due to the resonance line width and expected shift per QP trapped, it is possible that a low density of nonequilibrium QPs near the junction would lead to an inability to measure single QP trapping without QP injection and at low temperatures. There are a number of reasons that could contribute to this, such as the microwave packaging, flux-pinning holes in the ground plane, and the superconducting-gap profile. For the measurements presented in this work, we use a QCage, a microwave sample holder from QDevil. The QCage provides EMC-tight shielding by means of two layers of shielding: a Au-plated (Be-Cu) frame that forms a cavity and a sealed superconducting enclosure as seen in Fig. 10. The (Be-Cu)-Au inner-cavity parts are designed to have no line of sight into the cavity. The machined vent channels are all routed to prevent direct lines of sight. The only direct line of sight into the cavity around the chip is through the dielectric layers of the PCB stack and the coaxial cables. The chip, PCB, and cavity parts are sealed with an aluminum enclosure that superconducts at low T. The only line of sight through the aluminum casing is via the (Be-Cu)-Au side mounting rods and the coaxial connectors. It is possible that the EMC-tight shielding decreases the nonequilibrium QP density near the JJs, resulting in an inability to measure single QP trapping in real time.

We note that the flux-pinning holes surrounding the microwave circuit could also shield the SQUID from QPs in the ground plane. Since the flux-pinning holes are holes made in the superconducting ground plane, the exposed area of the holes is the conducting top InGaAs layer. This normal-metal layer can act as a QP trap. This can help reduce the QP density around the junctions.

We also consider the superconducting-gap profile of the structure, where the Al layer is sitting on a proximitized layer of an InAs 2DEG. The proximitized InAs has an induced superconducting gap lower than the superconducting parent gap of Al. It is possible that QPs relax into the proximitized InAs occupying the states close to the induced gap [77,78].

We emphasize that further investigation is required to determine with certainty the origin of the lack of QP trapping and clearing without deliberate QP injection and we hope that this will be the topic of future study.

APPENDIX F: EFFICIENCY OF CLEARING TONE

In this work, we utilize a high-frequency clearing tone to excite QP out of their traps. As we mention in the main text, the frequency chosen for the clearing tone is $f_{\text{clear}} = 18$ GHz, since it is near the third harmonic of the $\lambda/4$ resonator, where the admittance of the CPW is peaked. Ideally, the clearing tone should have an energy greater than the deepest Andreev trap, $hf_{\text{clear}} > \Delta_A(\tau = 1)$, to clear QPs from all Andreev traps directly to the continuum. At half flux, Eq. (1) results in a maximum $\Delta_A(\tau = 1)/h = 14.87$ GHz. However, Eq. (1) is a simple approximation for a one-dimensional conduction channel. If we consider the ABS modes plotted in Fig. 1(a) calculated using a 2D tight-binding model and we histogram the trap depth Δ_A at half flux, presented in Fig. 11, we see that a few of the modes have a trap depth $\Delta_A/h \gtrsim 18$ GHz. A few outliers are also present that correspond to long junction modes, with a trap depth that is significantly larger than 18 GHz. The clearing of QPs trapped in these modes with the applied 18 GHz will not be completely efficient and might involve mode-to-mode transitions rather than directmode-to-continuum clearing of QPs.

Moreover, the results shown in Fig. 5 show that the clearing and trapping times are of similar magnitude. As discussed in the text, a steady state can be achieved where the clearing and trapping events balance each other, with the Andreev states constantly being partially occupied even in the presence of the clearing tone. This finite QP occupation could be partly responsible for the inefficiency in the clearing tone.

APPENDIX G: FITTING TO THE MATTIS-BARDEEN THEORY

Following the work outlined in Refs. [65,79], the temperature dependence of the resonant frequency follows from the temperature dependence of the complex conductivity $\sigma = \sigma_1 + i\sigma_2$, where

$$\frac{\sigma_1(T,f)}{\sigma_n} = \frac{4\Delta_0}{hf} e^{-\Delta_0/k_BT} - 2e^{-\Delta_0/k_BT} e^{-hf/2k_BT} I_0\left(\frac{hf}{2k_BT}\right), \tag{G1}$$

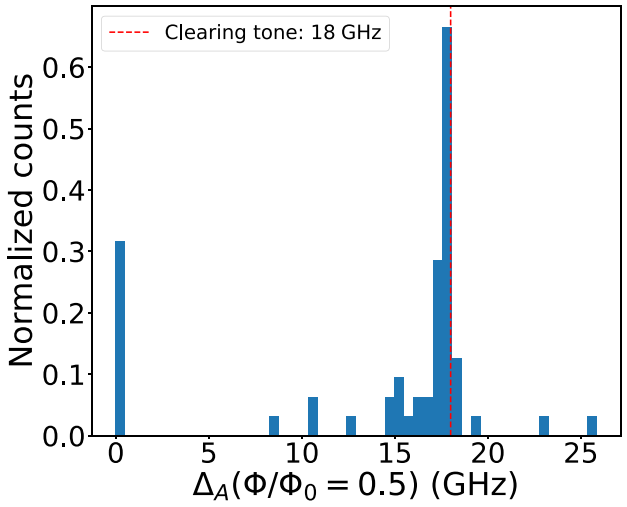

FIG. 11. A histogram of the Andreev-trap depth Δ_A at half flux extracted from the ABS modes calculated in Fig. 1(a).

$$\frac{\sigma_2(T,f)}{\sigma_n} = \frac{\pi\Delta_0}{hf}\left[1 - \sqrt{\frac{2\pi k_B T}{\Delta_0}}e^{-\Delta_0/k_B T} \times -2e^{-\Delta_0/k_B T}e^{-hf/2k_B T}I_0\left(\frac{hf}{2k_B T}\right)\right]. \quad \text{(G2)}$$

Here, σ_n is the normal-state conductivity, Δ_0 is the superconducting gap, k_B is Boltzmann's constant, f is the resonator frequency at low temperature, h is Planck's constant, and I_0 is the modified Bessel function of the first kind. We take the superconducting gap of Al to be $\Delta_0 = 210\ \mu$eV. It can be shown that in the thin-film local limit, the frequency response Δf_r to temperature is given by

$$\frac{\Delta f_r}{f_r} = -\frac{\alpha}{2}\left(1 - \sin(\phi(T,f))\sqrt{\frac{\sigma_1(T,f)^2 + \sigma_2(T,f)^2}{\sigma_1(0,f)^2 + \sigma_2(0,f)^2}}\right).$$

Fits to the data for the bare resonator and the SQUID at zero flux can be seen in Fig. 4(d). It is indeed seen that the data for the bare resonator and the SQUID at zero flux fit very well, while the SQUID at half flux deviates from this response due to the presence of QP trapping and clearing.

APPENDIX H: FITTING POWER-DEPENDENCE DATA

Here, we outline the derivation of the photon-number-dependent loss due to QP localization and excitation. Mobile QPs in the superconducting film can be localized to defects arising from disorder in the superconducting order parameter or from subgap bound states, acting as traps [47,48]. Following Refs. [11,70,80], one can write down a set of coupled equations that describes the changing densities of localized QPs (x_l) and mobile QPs (x_m). The coupled equations are a sum of terms that account for QP recombination, localization, excitation, and generation, being

$$\dot{x}_m = -\Gamma_{mm}x_m^2 - \Gamma_{ml}x_m x_l - \Gamma_{\rm loc}x_m + \Gamma_{\rm ex}x_l + g_m, \quad \text{(H1)}$$

$$\dot{x}_l = -\Gamma_{ll}x_l^2 - \Gamma_{ml}x_m x_l + \Gamma_{\rm loc}x_m - \Gamma_{\rm ex}x_l + g_l. \quad \text{(H2)}$$

The first two terms on the right-hand side of both equations describe QP recombination of two mobile QPs Γ_{mm}, two localized QPs Γ_{mm}, and a mobile QP and localized QP Γ_{ml}. The rates $\Gamma_{\rm loc}$ and $\Gamma_{\rm ex}$ describe localization and excitation to and from the subgap tail of the density of states. The generation of trapped and mobile QPs g_l and g_m are also included. Now considering the densities as having small deviations around constant steady-state densities, $x_l(t) = \bar{x}_l + \delta x_l(t)$ and $x_m(t) = \bar{x}_m + \delta x_m(t)$, we can examine the steady-state solution. Plugging these into Eqs. (H1) and (H2), one obtains

$$0 = -\Gamma_{mm}\bar{x}_m^2 - \Gamma_{ml}\bar{x}_m\bar{x}_l - \Gamma_{\rm loc}\bar{x}_m + \Gamma_{\rm ex}\bar{x}_l + g_m, \quad \text{(H3)}$$

$$0 = -\Gamma_{ll}\bar{x}_l^2 - \Gamma_{ml}\bar{x}_m\bar{x}_l + \Gamma_{\rm loc}\bar{x}_m - \Gamma_{\rm ex}\bar{x}_l + g_l. \quad \text{(H4)}$$

Assuming that $g_l = 0$, which is valid for high-energy QP-generating photons, that $\Gamma_{mm}x_m \ll \Gamma_{\rm loc}$, and that the excitation rate is proportional to the number of photons $\Gamma_{\rm ex} = \Gamma_0\bar{n}$, we obtain

$$0 = -\Gamma_{ml}\bar{x}_m\bar{x}_l - \Gamma_{\rm loc}\bar{x}_m + \Gamma_{\rm ex}\bar{x}_l + g_m, \quad \text{(H5)}$$

$$0 = -\Gamma_{ll}\bar{x}_l^2 - \Gamma_{ml}\bar{x}_m\bar{x}_l + \Gamma_{\rm loc}\bar{x}_m - \Gamma_{\rm ex}\bar{x}_l. \quad \text{(H6)}$$

Solving the latter equation for $\bar{x}_l$ and assuming $\Gamma_{ll}\Gamma_{\rm loc} \ll \Gamma_{ml}^2\bar{x}_m$, we find that

$$\bar{x}_l = \frac{\Gamma_{\rm loc}\bar{x}_m}{\Gamma_{ml}\bar{x}_m + \Gamma_{\rm ex}} \quad \text{(H7)}$$

Plugging this into Eq. (H5) and solving for $\bar{x}_m$, we find that

$$\bar{x}_m = \frac{g_m}{2\Gamma_{\rm loc}}\frac{1}{2}\left(1 + \sqrt{1 + 8\frac{\Gamma_{\rm loc}\Gamma_{\rm ex}}{g_m\Gamma_{ml}}}\right). \quad \text{(H8)}$$

Introducing the dimensionless ratio $\gamma = 2\Gamma_{\rm loc}\Gamma_0/g_m\Gamma_{ml}$, this is simplified to

$$\bar{x}_m = \frac{g_m}{2\Gamma_{\rm loc}}\left[1 + \frac{1}{2}\left(\sqrt{1 + 4\gamma\bar{n}} - 1\right)\right]. \quad \text{(H9)}$$

Plugging this into Eq. (H7),

$$\bar{x}_l = \frac{\Gamma_{\rm loc}}{\Gamma_{ml}} \frac{2}{\sqrt{4\gamma\bar{n}+1}+1}. \tag{H10}$$

The microwave loss can generically be written as an inverse sum of components due to temperature-dependent thermal QPs, the clearing of localized and mobile QPs, and temperature and power-independent residual loss mechanisms:

$$\frac{1}{Q_{\rm int}(T,\bar{n})} = \frac{1}{Q_0} + \frac{1}{Q(T)} + \frac{1}{Q(\bar{n})}. \tag{H11}$$

The power-dependent loss is due to the changing number of QPs via excitation and is proportional to the density of QPs, the coupling strength of the excitation tone, and the final density of states. Assuming that the final density of states and the density of localized QPs is greater than that of mobile QPs, for a similar coupling strength, the loss from localized QPs should dominate. Therefore,

$$Q(\bar{n}) = \frac{1}{\beta}\left[1 + \frac{\gamma\bar{n}}{1+\frac{1}{2}(\sqrt{1+4\gamma\bar{n}}-1)}\right]. \tag{H12}$$

Here, the prefactor β accounts for the proportionality of the loss to x_l and is proportional to the ratio of $\Gamma_{\rm loc}$ and Γ_{ml}. Fitting the data for β and γ thus allows us to make a conclusion about the trapping rates in the different devices reported here.

APPENDIX I: LIMITATIONS IN $t_{\rm trap}$ AND $t_{\rm clear}$ EXTRACTION

In Fig. 5, we present time-domain measurements related to the trapping and clearing of QPs. As described in the main text, $t_{\rm trap}$ and $t_{\rm clear}$ are extracted by fitting the clearing-tone-induced jumps and drops in I or Q to an exponential function [47]. At $V_{\rm inj} < 2$ mV and $T < 225$ mK, given our sensitivity to QP poisoning events, the QP density in the system is low enough that there is not a significant amount of QPs occupying the Andreev traps. Therefore, the response in I and Q to the clearing tone is either not visible or is very minimal, given our signal-to-noise ratio, which does not allow for a reliable fit to extract clearing or trapping times. This is seen in Fig. 12, where the response of I to the clearing-tone pulse is plotted for $V_{\rm inj} = 0$ mV, where the jumps are not well defined, along with $V_{\rm inj} = 2$ mV, where the jumps are more defined, allowing for a reliable extraction of clearing and trapping times. Hence, we only present trapping and clearing time for $V_{\rm inj} \geq 2$ mV and $T \geq 225$ mK, where the jumps and drops in I and Q are prominent enough that we can obtain a reliable fit to extract the trapping and clearing times.

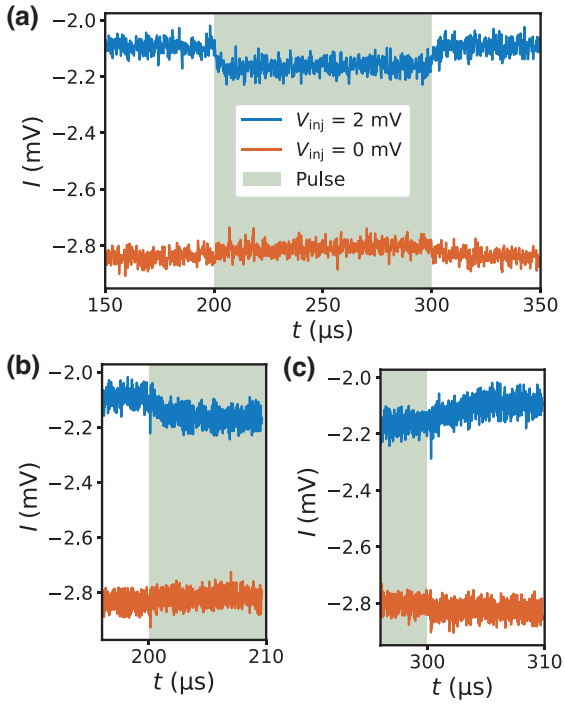

FIG. 12. (a) An example measurement of the I response over time t for two different values of $V_{\rm inj}$ at $\Phi_{\rm ext}/\Phi_0 = 0.5$ and at a temperature of $T = 15$ mKe. The region where the pulse is maximum is shaded in green. (b),(c) Regions that we fit to extract the clearing and trapping times are shown in (b) and (c) respectively. For the injector voltage biases of $V_{\rm inj} = 2$ mV and $V_{\rm inj} = 0$ mV.

APPENDIX J: PHENOMENOLOGICAL MODEL FOR QP DENSITY

We present a simplified version of the analysis mentioned in Appendix H in order to fit the clearing and trapping times as a function of the temperature and the injector voltage bias. We use the reduced QP density $x(t)$ in the superconducting region of the device in the vicinity of the JJs, $x = n_{\rm QP}/n_{\rm CP}$, where $n_{\rm QP}$ is the density of QPs normalized to the density of Cooper pairs $n_{\rm CP}$. Again, the equation for the reduced QP density has the form [11,80]

$$\dot{x} = -rx^2 - sx - px + g, \tag{J1}$$

where we now consider only trapped QPs. Here, r and s are the recombination and trapping rates for QPs in the superconducting region, p is the trapping rate for the JJ, and g is the QP generation rate due to Cooper-pair breaking by phonons [20].

In our analysis, we assume that the reduced QP density $\bar{x}$ is stationary and according to Eq. (J1), depends on the QP generation rate g:

$$\bar{x} = \frac{\sqrt{(s+p)^2+4gr}-s-p}{2r}. \tag{J2}$$

We note that by making the substitution

$$s + p \to \Gamma_{ml}\bar{x}_m + \Gamma_{\rm ex}, g \to \Gamma_{\rm loc}\bar{x}_m, r \to \Gamma_{ll}, \tag{J3}$$

one recovers the model presented in Appendix H and Ref. [70]. However, when the injector is biased to inject QPs, we use $\bar{x} = \sqrt{g/r}$ for a strong generation rate $gr \gg s^2$ and $\bar{x} = g/s$ for weak generation $gr \ll s^2$. Here, we assume that $s \gg p$, i.e., that QP poisoning in the junctions is not the main mechanism for QP trapping. The generation rate has been estimated in Ref. [20] as $g \propto \sqrt{(eV_{\rm inj}/\Delta)^2 - 1}$. Assuming that the QP generation rate is not high such that $gr \lesssim s$, for $V_{\rm inj} \gg \Delta/e$, we have

$$\bar{x} = \frac{g}{s} \propto V_{\rm inj}. \tag{J4}$$

When no QPs are injected by the injector junction, the QP density is defined by the thermal distribution, $\bar{x} = x_{\rm eq}(T)$, given by Eq. (5).

We write the equation for the number of trapped QPs in the ABSs of the junction n_A as [70]

$$\dot{n}_A = -r_{{\rm qp},A} x n_A - r_A n_A^2 - \gamma_{\rm exc} n_A + pSx + g_A, \tag{J5}$$

where $r_{{\rm qp},A}$ is the recombination rate of one QP in the superconducting region and one trapped QP in the junction, r_A is the recombination of trapped QPs, S is the area of the junction, $\gamma_{\rm exc}$ is the excitation rate of trapped QPs by the clearing tone, and g_A is the generation rate of trapped QPs from other sources. We again treat the rates in Eq. (J5) as phenomenological parameters.

We first evaluate the steady-state value of the trapped QPs. We take $\dot{n}_A = 0$ in Eq. (J5) and we obtain

$$\bar{n}_A = \frac{pS\bar{x} + g_A}{r_{\rm qp,A}\bar{x} + \gamma_{\rm exc}}. \tag{J6}$$

Here, we assume that the recombination term $r_A n_A^2$ of trapped QPs provides a negligible contribution. The number of photons in the resonator defines the excitation rate $\gamma_{\rm exc}$ and, consequently, the number of trapped QPs $\bar{n}_A$. As the clearing pulse is turned on and off, the number of QPs will switch between two values given by Eq. (J6) with and without $\gamma_{\rm exc}$.

Next, we linearize Eq. (J5) in small changes of the trapped QP number:

$$\delta\dot{n}_A = -\Gamma\delta n_A, \quad \Gamma = r_{\rm qp,A}x + 2r_A n_A + \gamma_{\rm exc}. \tag{J7}$$

We can disregard $2r_A n_A$, which represents recombination of trapped QPs. We find that the trapping, $t_{\rm trap}$, and clearing, $t_{\rm clear}$, times are determined by the reduced QS density as

$$t_{\rm trap} = \frac{1}{r_{\rm qp,A}\bar{x}}, \quad t_{\rm clear} = \frac{1}{r_{\rm qp,A}\bar{x} + \gamma_{\rm exc}}. \tag{J8}$$

Because of the additional term $\gamma_{\rm exc}$ representing excitation of trapped QPs by the clearing tone, the clearing time is shorter than the trapping time, $t_{\rm clear} < t_{\rm trap}$. In the absence of the injection voltage, $V_{\rm inj} = 0$, the QP density $\bar{x} = x_{\rm eq}(T)$ is given by Eq. (5). The data shown in Fig. 5(e) are consistent with the scaling in Eq. (J8), as both the trapping and clearing times are seen to scale with $x_{\rm eq}(T)$ given by Eq. (5) if Δ is suppressed by a factor of 1.5. The reason for such a gap is unclear and requires further investigation. With QP injection, we use $\bar{x} \propto V_{\rm inj}$ to fit the curves for the trapping and clearing times [see Eq. (J4)] and find good agreement with the data, as shown in Fig. 5(d).

[1] J. M. Martinis, M. Ansmann, and J. Aumentado, Energy Decay in Superconducting Josephson-Junction Qubits from Nonequilibrium Quasiparticle Excitations, Phys. Rev. Lett. **103**, 097002 (2009).

[2] A. P. Vepsäläinen, A. H. Karamlou, J. L. Orrell, A. S. Dogra, B. Loer, F. Vasconcelos, D. K. Kim, A. J. Melville, B. M. Niedzielski, J. L. Yoder, S. Gustavsson, J. A. Formaggio, B. A. VanDevender, and W. D. Oliver, Impact of ionizing radiation on superconducting qubit coherence, Nature **584**, 551 (2020).

[3] J. M. Martinis, Saving superconducting quantum processors from decay and correlated errors generated by gamma and cosmic rays, npj Quantum Inf. **7**, 90 (2021).

[4] K. Serniak, M. Hays, G. de Lange, S. Diamond, S. Shankar, L. D. Burkhart, L. Frunzio, M. Houzet, and M. H. Devoret, Hot Nonequilibrium Quasiparticles in Transmon Qubits, Phys. Rev. Lett. **121**, 157701 (2018).

[5] L. I. Glazman and G. Catelani, Bogoliubov quasiparticles in superconducting qubits, SciPost Phys. Lect. Notes, 31 (2021).

[6] S. Diamond, V. Fatemi, M. Hays, H. Nho, P. D. Kurilovich, T. Connolly, V. R. Joshi, K. Serniak, L. Frunzio, L. I. Glazman, and M. H. Devoret, Distinguishing Parity-Switching Mechanisms in a Superconducting Qubit, PRX Quantum **3**, 040304 (2022).

[7] M. Cheng, R. M. Lutchyn, and S. Das Sarma, Topological protection of Majorana qubits, Phys. Rev. B **85**, 165124 (2012).

[8] D. Rainis and D. Loss, Majorana qubit decoherence by quasiparticle poisoning, Phys. Rev. B **85**, 174533 (2012).

[9] J. Aumentado, M. W. Keller, J. M. Martinis, and M. H. Devoret, Nonequilibrium Quasiparticles and 2e Periodicity in Single-Cooper-Pair Transistors, Phys. Rev. Lett. **92**, 066802 (2004).

[10] G. Catelani, J. Koch, L. Frunzio, R. J. Schoelkopf, M. H. Devoret, and L. I. Glazman, Quasiparticle Relaxation of Superconducting Qubits in the Presence of Flux, Phys. Rev. Lett. **106**, 077002 (2011).

[11] C. Wang, Y. Y. Gao, I. M. Pop, U. Vool, C. Axline, T. Brecht, R. W. Heeres, L. Frunzio, M. H. Devoret, G. Catelani, L. I. Glazman, and R. J. Schoelkopf, Measurement and control of quasiparticle dynamics in a superconducting qubit, Nat. Commun. **5**, 5836 (2014).

[12] R. Barends, J. Wenner, M. Lenander, Y. Chen, R. C. Bialczak, J. Kelly, E. Lucero, P. O'Malley, M. Mariantoni, D. Sank, H. Wang, T. C. White, Y. Yin, J. Zhao, A. N. Cleland, J. M. Martinis, and J. J. A. Baselmans, Minimizing quasiparticle generation from stray infrared light in superconducting quantum circuits, Appl. Phys. Lett. **99**, 113507 (2011).

[13] L. Cardani *et al.*, Reducing the impact of radioactivity on quantum circuits in a deep-underground facility, Nat. Commun. **12**, 2733 (2021).

[14] C. D. Wilen, S. Abdullah, N. A. Kurinsky, C. Stanford, L. Cardani, G. D'Imperio, C. Tomei, L. Faoro, L. B. Ioffe, C. H. Liu, A. Opremcak, B. G. Christensen, J. L. DuBois, and R. McDermott, Correlated charge noise and relaxation errors in superconducting qubits, Nature **594**, 369 (2021).

[15] M. McEwen *et al.*, Resolving catastrophic error bursts from cosmic rays in large arrays of superconducting qubits, Nat. Phys. **18**, 107 (2022).

[16] C. Kurter, C. E. Murray, R. T. Gordon, B. B. Wymore, M. Sandberg, R. M. Shelby, A. Eddins, V. P. Adiga, A. D. K. Finck, E. Rivera, A. A. Stabile, B. Trimm, B. Wacaser, K. Balakrishnan, A. Pyzyna, J. Sleight, M. Steffen, and K. Rodbell, Quasiparticle tunneling as a probe of Josephson junction barrier and capacitor material in superconducting qubits, npj Quantum Inf. **8**, 31 (2022).

[17] R.-P. Riwar, A. Hosseinkhani, L. D. Burkhart, Y. Y. Gao, R. J. Schoelkopf, L. I. Glazman, and G. Catelani, Normal-metal quasiparticle traps for superconducting qubits, Phys. Rev. B **94**, 104516 (2016).

[18] I. Nsanzineza and B. Plourde, Trapping a Single Vortex and Reducing Quasiparticles in a Superconducting Resonator, Phys. Rev. Lett. **113**, 117002 (2014).

[19] M. Taupin, I. M. Khaymovich, M. Meschke, A. S. Mel'nikov, and J. P. Pekola, Tunable quasiparticle trapping in Meissner and vortex states of mesoscopic superconductors, Nat. Commun. **7**, 10977 (2016).

[20] U. Patel, I. V. Pechenezhskiy, B. L. T. Plourde, M. G. Vavilov, and R. McDermott, Phonon-mediated quasiparticle poisoning of superconducting microwave resonators, Phys. Rev. B **96**, 220501 (2017).

[21] W. Eisenmenger and A. H. Dayem, Quantum Generation and Detection of Incoherent Phonons in Superconductors, Phys. Rev. Lett. **18**, 125 (1967).

[22] O. O. Otelaja, J. B. Hertzberg, M. Aksit, and R. D. Robinson, Design and operation of a microfabricated phonon spectrometer utilizing superconducting tunnel junctions as phonon transducers, New J. Phys. **15**, 043018 (2013).

[23] G. de Lange, B. van Heck, A. Bruno, D. J. van Woerkom, A. Geresdi, S. R. Plissard, E. P. A. M. Bakkers, A. R. Akhmerov, and L. DiCarlo, Realization of Microwave Quantum Circuits Using Hybrid Superconducting-Semiconducting Nanowire Josephson Elements, Phys. Rev. Lett. **115**, 127002 (2015).

[24] T. W. Larsen, K. D. Petersson, F. Kuemmeth, T. S. Jespersen, P. Krogstrup, J. Nygård, and C. M. Marcus, Semiconductor-Nanowire-Based Superconducting Qubit, Phys. Rev. Lett. **115**, 127001 (2015).

[25] F. Luthi, T. Stavenga, O. W. Enzing, A. Bruno, C. Dickel, N. K. Langford, M. A. Rol, T. S. Jespersen, J. Nygård, P. Krogstrup, and L. DiCarlo, Evolution of Nanowire Transmon Qubits and Their Coherence in a Magnetic Field, Phys. Rev. Lett. **120**, 100502 (2018).

[26] A. Kringhøj, L. Casparis, M. Hell, T. W. Larsen, F. Kuemmeth, M. Leijnse, K. Flensberg, P. Krogstrup, J. Nygård, K. D. Petersson, and C. M. Marcus, Anharmonicity of a superconducting qubit with a few-mode josephson junction, Phys. Rev. B **97**, 060508 (2018).

[27] L. Casparis, M. R. Connolly, M. Kjaergaard, N. J. Pearson, A. Kringhøj, T. W. Larsen, F. Kuemmeth, T. Wang, C. Thomas, S. Gronin, G. C. Gardner, M. J. Manfra, C. M. Marcus, and K. D. Petersson, Superconducting gatemon qubit based on a proximitized two-dimensional electron gas, Nat. Nanotechnol. **13**, 915 (2018).

[28] L. Casparis, T. W. Larsen, M. S. Olsen, F. Kuemmeth, P. Krogstrup, J. Nygård, K. D. Petersson, and C. M. Marcus, Gatemon Benchmarking and Two-Qubit Operations, Phys. Rev. Lett. **116**, 150505 (2016).

[29] J. O'Connell Yuan, K. S. Wickramasinghe, W. M. Strickland, M. C. Dartiailh, K. Sardashti, M. Hatefipour, and J. Shabani, Epitaxial superconductor-semiconductor two-dimensional systems for superconducting quantum circuits, J. Vac. Sci. Technol. A **39**, 033407 (2021).

[30] T. W. Larsen, M. E. Gershenson, L. Casparis, A. Kringhøj, N. J. Pearson, R. P. G. McNeil, F. Kuemmeth, P. Krogstrup, K. D. Petersson, and C. M. Marcus, Parity-Protected Superconductor-Semiconductor Qubit, Phys. Rev. Lett. **125**, 056801 (2020).

[31] M. Hays, V. Fatemi, K. Serniak, D. Bouman, S. Diamond, G. de Lange, P. Krogstrup, J. Nygård, A. Geresdi, and M. H. Devoret, Continuous monitoring of a trapped superconducting spin, Nat. Phys. **16**, 1103 (2020).

[32] M. Hays, V. Fatemi, D. Bouman, J. Cerrillo, S. Diamond, K. Serniak, T. Connolly, P. Krogstrup, J. Nygård, A. L. Yeyati, A. Geresdi, and M. H. Devoret, Coherent manipulation of an Andreev spin qubit, Science **373**, 430 (2021).

[33] A. Danilenko, D. Sabonis, G. W. Winkler, O. Erlandsson, P. Krogstrup, and C. M. Marcus, Few-mode to mesoscopic junctions in gatemon qubits, arXiv:2209.03688 (2022).

[34] A. Hertel, M. Eichinger, L. O. Andersen, D. M. T. van Zanten, S. Kallatt, P. Scarlino, A. Kringhøj, J. M. Chavez-Garcia, G. C. Gardner, S. Gronin, M. J. Manfra, A. Gyenis, M. Kjaergaard, C. M. Marcus, and K. D. Petersson, Gate-tunable transmon using selective-area-grown superconductor-semiconductor hybrid structures on silicon, arXiv:2202.10860 (2022).

[35] D. Phan, P. Falthansl-Scheinecker, U. Mishra, W. M. Strickland, D. Langone, J. Shabani, and A. P. Higginbotham, Semiconductor quantum-limited amplifier, arXiv:2206.05746 (2022).

[36] L. Casparis, N. J. Pearson, A. Kringhøj, T. W. Larsen, F. Kuemmeth, J. Nygård, P. Krogstrup, K. D. Petersson, and C. M. Marcus, Voltage-controlled superconducting quantum bus, Phys. Rev. B **99**, 085434 (2019).

[37] Z. Qi, H. Xie, J. Shabani, V. E. Manucharyan, A. Levchenko, and M. G. Vavilov, Controlled-Z gate for

transmon qubits coupled by semiconductor junctions, Phys. Rev. B **97**, 134518 (2018).

[38] K. Sardashti, M. C. Dartiailh, J. Yuan, S. Hart, P. Gumann, and J. Shabani, Voltage-tunable superconducting resonators: A platform for random access quantum memory, IEEE Trans. Quantum Eng. **1**, 1 (2020).

[39] W. M. Strickland, B. H. Elfeky, J. O. Yuan, W. F. Schiela, P. Yu, D. Langone, M. G. Vavilov, V. E. Manucharyan, and J. Shabani, Superconducting Resonators with Voltage-Controlled Frequency and Nonlinearity, Phys. Rev. Appl. **19**, 034021 (2023).

[40] W. Mayer, M. C. Dartiailh, J. Yuan, K. S. Wickramasinghe, E. Rossi, and J. Shabani, Gate controlled anomalous phase shift in Al/InAs Josephson junctions, Nat. Commun. **11**, 212 (2020).

[41] A. Fornieri, A. M. Whiticar, F. Setiawan, E. Portolés, A. C. C. Drachmann, A. Keselman, S. Gronin, C. Thomas, T. Wang, R. Kallaher, G. C. Gardner, E. Berg, M. J. Manfra, A. Stern, C. M. Marcus, and F. Nichele, Evidence of topological superconductivity in planar Josephson junctions, Nature **569**, 89 (2019).

[42] B. H. Elfeky, N. Lotfizadeh, W. F. Schiela, W. M. Strickland, M. Dartiailh, K. Sardashti, M. Hatefipour, P. Yu, N. Pankratova, H. Lee, V. E. Manucharyan, and J. Shabani, Local control of supercurrent density in epitaxial planar Josephson junctions, Nano Lett. **21**, 8274 (2021), publisher: American Chemical Society.

[43] A. Banerjee, O. Lesser, M. A. Rahman, H. R. Wang, M. R. Li, A. Kringhøj, A. M. Whiticar, A. C. C. Drachmann, C. Thomas, T. Wang, M. J. Manfra, E. Berg, Y. Oreg, A. Stern, and C. M. Marcus, Signatures of a topological phase transition in a planar Josephson junction, arxiv arXiv:2201.03453 (2022), publisher: arXiv Version Number: 1.

[44] C. W. J. Beenakker, Quantum transport in semiconductor-superconductor microjunctions, Phys. Rev. B **46**, 12841 (1992).

[45] M. C. Dartiailh, J. J. Cuozzo, B. H. Elfeky, W. Mayer, J. Yuan, K. S. Wickramasinghe, E. Rossi, and J. Shabani, Missing Shapiro steps in topologically trivial Josephson junction on InAs quantum well, Nat. Commun. **12**, 78 (2021).

[46] B. H. Elfeky, J. J. Cuozzo, N. Lotfizadeh, W. F. Schiela, S. M. Farzaneh, W. M. Strickland, D. Langone, E. Rossi, and J. Shabani, Evolution of 4π-Periodic Supercurrent in the Presence of an In-Plane Magnetic Field, ACS Nano **17**, 4650 (2023).

[47] E. M. Levenson-Falk, F. Kos, R. Vijay, L. Glazman, and I. Siddiqi, Single-Quasiparticle Trapping in Aluminum Nanobridge Josephson Junctions, Phys. Rev. Lett. **112**, 047002 (2014).

[48] J. T. Farmer, A. Zarassi, D. M. Hartsell, E. Vlachos, H. Zhang, and E. M. Levenson-Falk, Continuous real-time detection of quasiparticle trapping in aluminum nanobridge Josephson junctions, Appl. Phys. Lett. **119**, 122601 (2021).

[49] J. T. Farmer, A. Zarassi, S. Shanto, D. Hartsell, and E. M. Levenson-Falk, Electron-phonon interactions in the Andreev bound states of aluminum nanobridge Josephson junctions, arXiv:2211.16765 (2022).

[50] J. Shabani, M. Kjaergaard, H. J. Suominen, Y. Kim, F. Nichele, K. Pakrouski, T. Stankevic, R. M. Lutchyn, P. Krogstrup, R. Feidenhans'l, S. Kraemer, C. Nayak, M. Troyer, C. M. Marcus, and C. J. Palmstrøm, Two-dimensional epitaxial superconductor-semiconductor heterostructures: A platform for topological superconducting networks, Phys. Rev. B **93**, 155402 (2016).

[51] K. S. Wickramasinghe, W. Mayer, J. Yuan, T. Nguyen, L. Jiao, V. Manucharyan, and J. Shabani, Transport properties of near surface InAs two-dimensional heterostructures, Appl. Phys. Lett. **113**, 262104 (2018).

[52] J. Yuan, M. Hatefipour, B. A. Magill, W. Mayer, M. C. Dartiailh, K. Sardashti, K. S. Wickramasinghe, G. A. Khodaparast, Y. H. Matsuda, Y. Kohama, Z. Yang, S. Thapa, C. J. Stanton, and J. Shabani, Experimental measurements of effective mass in near-surface InAs quantum wells, Phys. Rev. B **101**, 205310 (2020).

[53] W. M. Strickland, M. Hatefipour, D. Langone, S. M. Farzaneh, and J. Shabani, Controlling fermi level pinning in near-surface InAs quantum wells, Appl. Phys. Lett. **121**, 092104 (2022).

[54] V. Iaia, J. Ku, A. Ballard, C. P. Larson, E. Yelton, C. H. Liu, S. Patel, R. McDermott, and B. L. T. Plourde, Phonon downconversion to suppress correlated errors in superconducting qubits, Nat. Commun. **13**, 6425 (2022).

[55] A. Bargerbos, L. J. Splitthoff, M. Pita-Vidal, J. J. Wesdorp, Y. Liu, P. Krogstrup, L. P. Kouwenhoven, C. K. Andersen, and L. Grünhaupt, Mitigation of quasiparticle loss in superconducting qubits by phonon scattering, arXiv:2207.12754 (2022).

[56] S. Probst, F. B. Song, P. A. Bushev, A. V. Ustinov, and M. Weides, Efficient and robust analysis of complex scattering data under noise in microwave resonators, Rev. Sci. Instrum. **86**, 024706 (2015).

[57] F. Nichele, E. Portolés, A. Fornieri, A. Whiticar, A. Drachmann, S. Gronin, T. Wang, G. Gardner, C. Thomas, A. Hatke, M. Manfra, and C. Marcus, Relating Andreev Bound States and Supercurrents in Hybrid Josephson Junctions, Phys. Rev. Lett. **124**, 226801 (2020).

[58] M. C. Dartiailh, W. Mayer, J. Yuan, K. S. Wickramasinghe, A. Matos-Abiague, I. Žutić, and J. Shabani, Phase Signature of Topological Transition in Josephson Junctions, Phys. Rev. Lett. **126**, 036802 (2021).

[59] N. A. Masluk, I. M. Pop, A. Kamal, Z. K. Minev, and M. H. Devoret, Microwave Characterization of Josephson Junction Arrays: Implementing a Low Loss Superinductance, Phys. Rev. Lett. **109**, 137002 (2012).

[60] E. M. Levenson-Falk, Ph.D. thesis, University of California, Berkeley, 2013.

[61] E. M. Levenson-Falk, R. Vijay, and I. Siddiqi, Nonlinear microwave response of aluminum weak-link Josephson oscillators, Appl. Phys. Lett. **98**, 123115 (2011).

[62] F. Nichele, A. C. C. Drachmann, A. M. Whiticar, E. C. T. O'Farrell, H. J. Suominen, A. Fornieri, T. Wang, G. C. Gardner, C. Thomas, A. T. Hatke, P. Krogstrup, M. J. Manfra, K. Flensberg, and C. M. Marcus, Scaling of Majorana Zero-Bias Conductance Peaks, Phys. Rev. Lett. **119**, 136803 (2017).

[63] A. Palacios-Laloy, F. Nguyen, F. Mallet, P. Bertet, D. Vion, and D. Esteve, Tunable Resonators for Quantum Circuits, J. Low. Temp. Phys. **151**, 1034 (2008).

[64] M. Sandberg, C. M. Wilson, F. Persson, T. Bauch, G. Johansson, V. Shumeiko, T. Duty, and P. Delsing, Tuning the field in a microwave resonator faster than the photon lifetime, Appl. Phys. Lett. **92**, 203501 (2008).

[65] J. Gao, Ph.D. thesis, California Institute of Technology, 2008.

[66] J. Zmuidzinas, Superconducting Microresonators: Physics and Applications, Annu. Rev. Condens. Matter Phys. **3**, 169 (2012).

[67] X. Pan, Y. Zhou, H. Yuan, L. Nie, W. Wei, L. Zhang, J. Li, S. Liu, Z. H. Jiang, G. Catelani, L. Hu, F. Yan, and D. Yu, Engineering superconducting qubits to reduce quasiparticles and charge noise, Nat. Commun. **13**, 7196 (2022).

[68] J. Wenner, R. Barends, R. C. Bialczak, Y. Chen, J. Kelly, E. Lucero, M. Mariantoni, A. Megrant, P. J. J. O'Malley, D. Sank, A. Vainsencher, H. Wang, T. C. White, Y. Yin, J. Zhao, A. N. Cleland, and J. M. Martinis, Surface loss simulations of superconducting coplanar waveguide resonators, Appl. Phys. Lett. **99**, 113513 (2011).

[69] J. M. Sage, V. Bolkhovsky, W. D. Oliver, B. Turek, and P. B. Welander, Study of loss in superconducting coplanar waveguide resonators, J. Appl. Phys. **109**, 063915 (2011).

[70] L. Grünhaupt, N. Maleeva, S. T. Skacel, M. Calvo, F. Levy-Bertrand, A. V. Ustinov, H. Rotzinger, A. Monfardini, G. Catelani, and I. M. Pop, Loss Mechanisms and Quasiparticle Dynamics in Superconducting Microwave Resonators Made of Thin-Film Granular Aluminum, Phys. Rev. Lett. **121**, 117001 (2018).

[71] C. W. Groth, M. Wimmer, A. R. Akhmerov, and X. Waintal, KWANT: A software package for quantum transport, New J. Phys. **16**, 063065 (2014).

[72] C. M. Moehle, P. K. Rout, N. A. Jainandunsing, D. Kuiri, C. T. Ke, D. Xiao, C. Thomas, M. J. Manfra, M. P. Nowak, and S. Goswami, Controlling Andreev Bound States with the Magnetic Vector Potential, Nano Lett. **22**, 8601 (2022).

[73] Z. K. Minev, T. G. McConkey, J. Drysdale, P. Shah, D. Wang, M. Facchini, G. Harper, J. Blair, H. Zhang, N. Lanzillo, S. Mukesh, W. Shanks, C. Warren, and J. M. Gambetta, QISKIT METAL: An open-source framework for quantum device design & analysis (2021).

[74] ANSYS HFSS software: http://www.ansoft.com/products/hf/hfss/.

[75] R. N. Simons, in *Coplanar Waveguide Circuits, Components, and Systems* (John Wiley & Sons Ltd, Hoboken, New Jersey, 2001), Chap. 2, p. 11.

[76] S. B. Kaplan, C. C. Chi, D. N. Langenberg, J. J. Chang, S. Jafarey, and D. J. Scalapino, Quasiparticle and phonon lifetimes in superconductors, Phys. Rev. B **14**, 4854 (1976).

[77] G. Marchegiani, L. Amico, and G. Catelani, Quasiparticles in Superconducting Qubits with Asymmetric Junctions, PRX Quantum **3**, 040338 (2022).

[78] T. Connolly, P. D. Kurilovich, S. Diamond, H. Nho, C. G. L. Bøttcher, L. I. Glazman, V. Fatemi, and M. H. Devoret, Coexistence of nonequilibrium density and equilibrium energy distribution of quasiparticles in a superconducting qubit, arXiv:2302.12330 [cond-mat, physics:quant-ph] (2023).

[79] D. C. Mattis and J. Bardeen, Theory of the anomalous skin effect in normal and superconducting metals, Phys. Rev. **111**, 412 (1958).

[80] A. Rothwarf and B. N. Taylor, Measurement of Recombination Lifetimes in Superconductors, Phys. Rev. Lett. **19**, 27 (1967).